

NEUTRAL B MESON FLAVOR TAGGING FOR BELLE II

Moritz J. Gelb

MASTERARBEIT

an der Fakultät für Physik des
Karlsruher Institut für Technologie (KIT)

Institut für Experimentelle Kernphysik

Referent: Prof. Dr. Thomas Kuhr

Korreferent: Prof. Dr. Michael Feindt

APRIL 2015

Deutsche Zusammenfassung

Das Belle Experiment in Tsukuba, Japan wurde konzipiert, um das Standardmodell der Teilchenphysik zu validieren und nach „Neuer Physik“ zu suchen. Durch die Kollision von Elektronen und Positronen bei einer Schwerpunktsenergie die der $\Upsilon(4S)$ Resonanz entspricht entstehen Paare von gebundenen b -Quark-Zuständen, sogenannte B -Mesonen. Bis zum Ende des Experiments 2010 wurden insgesamt mehr als 772 Millionen $B\bar{B}$ -Paare erzeugt.

Einer der größten Erfolge des Belle Experiments war die Messung der direkten und mischungsinduzierten CP-Verletzung in verschiedenen Zerfallsmodi [1, 2]. Dies führte schließlich zum Nobelpreis für Kobayashi und Maskawa, die Jahrzehnte zuvor das theoretische Konzept der CP-Verletzung eingeführt hatten [3]. Das breit angelegte Experiment konnte aber auch noch andere Erfolge vermelden, wie etwa die Messung des Zerfalls $B^+ \rightarrow \tau^+ \nu_\tau$ [4], die Mischung von D^0 -Mesonen [5] oder die Entdeckung der $X(3872)$ Resonanz [6].

Das nachfolgende Belle II Experiment wird verstärkt nach Prozessen neuer Physik suchen, aber auch schon bekannte Parameter noch präziser vermessen. Um die dafür benötigte 40-fach höhere instantane Luminosität zu erreichen, wird sowohl der Beschleuniger als auch der Detektor aufgerüstet. Die Datennahme wird voraussichtlich 2018 beginnen.

Ein wichtiges Analysewerkzeug, das beispielsweise bei der Messung der mischungsinduzierten CP-Verletzung im „Goldenen Kanal“ $B^0 \rightarrow J/\Psi K_S^0$ eingesetzt wird, ist das Flavor Tagging [7]. Bei der Messung wird eines der beiden B -Mesonen in einem CP-Eigenzustand rekonstruiert (siehe Abb. 0.1). Dabei ist aber unklar, welchen Flavor das rekonstruierte Meson hat. Durch die Untersuchung verschiedener Kategorien von Endzustandsteilchen des zweiten B -Mesons auf der sogenannten Tag-Seite kann der Flavor beider Mesonen bestimmt werden. Beispielsweise entsteht bei einem semileptonischen B -Zerfall ein positiv (negativ) geladenes Lepton das auf ein $B^0(\bar{B}^0)$ -Meson hinweist.

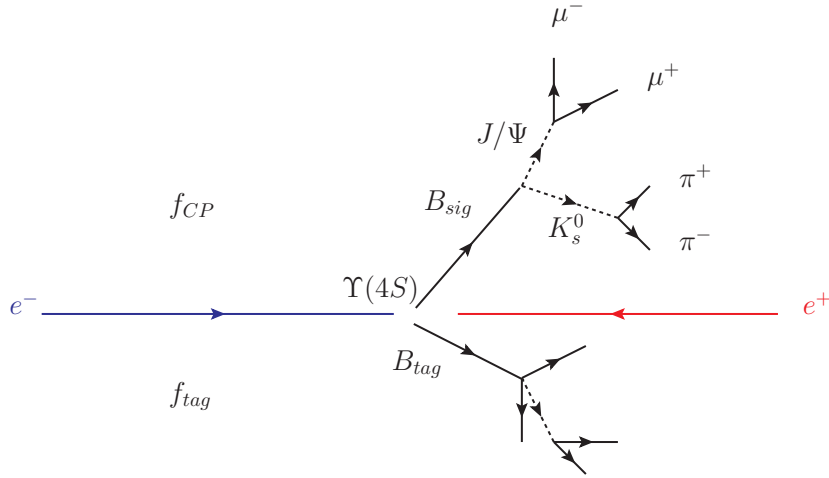


Abbildung 0.1.: Rekonstruktion des CP-Eigenzustandes auf der Signal-Seite f_{CP} . Die Spuren der Tag-Seite f_{tag} werden für das Flavor Tagging verwendet.

In dieser Arbeit wird die Implementierung des Flavor Taggings in das Software Framework des Belle II Experiments vorgestellt. Dabei durchläuft jedes Event einen zweistufigen Prozess. In der ersten Stufe werden die Spuren der Tag-Seite analysiert. Die Spuren werden in den einzelnen Kategorien anhand ihrer Eigenschaften, z.B. ihrer Kinematik, mittels multivariater Methoden bewertet. Der Flavor ergibt sich dabei aus der Ladung der Spur. In einer zweiten Ebene werden die Kandidaten der einzelnen Kategorien zu einem Ergebnis kombiniert. Dies geschieht durch eine weitere multivariate Methode. Das finale Ergebnis besteht zum einen aus dem Flavor q der die Werte $+1$ und -1 für ein B^0 (\bar{B}^0) annehmen kann, zum anderen erhält man den Dilution-Faktor r der zwischen 0 und 1 liegt und angibt wie sicher sich die Methode bei ihrer Entscheidung ist. Die finale Ausgabe des Taggers auf simulierten Events ist in Abb. 0.2 dargestellt. Das Maximum bei einem Wert um 0 entspricht Events für die keine oder nur eine sehr unsichere Aussage getroffen werden konnte. Je weiter außerhalb sich die Ergebnisse befinden, desto sicherer ist die Tagger Aussage.

Um die Leistungsfähigkeit des Algorithmus zu bestimmen, wird die sogenannte effektive Effizienz betrachtet. In dieser Arbeit konnte eine effektive Effizienz auf simulierten Events von 32.44 % erreicht werden, sie liegt somit etwa 3.1 % über der des Belle Experiments.

Zudem wird das Flavor Tagging erweitert. Bei dem bisherigen Ansatz steht keine Information über rekonstruierte D - oder B -Mesonen zur Verfügung. Dennoch kann diese Information bei der Bestimmung des Flavors hilfreich sein. Daher wurde ein schon bestehendes Analysewerkzeug in das Flavor Tagging integriert. Die Full Event Interpretation verfolgt einen rein exklusiven Ansatz, d.h. die Endzustandsteilchen der Tag-Seite werden in verschiedenen Zerfallsmodi rekonstruiert [8]. Diese

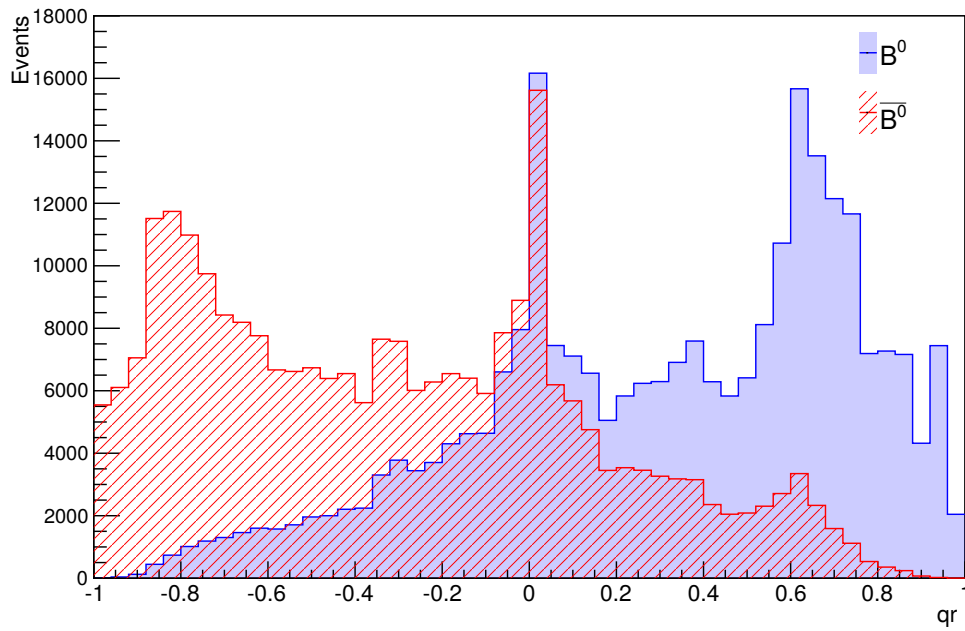


Abbildung 0.2.: Finale Ausgabe des Flavor Taggings auf simulierten Monte Carlo Daten. Der Tagger wurde auf eine Million B -Mesonpaare nach korrekter Rekonstruktion der Signal-Seite trainiert und angewendet. Die Ausgabe für $B^0(\bar{B}^0)$ -Mesonen ist in blau (rot) dargestellt.

zusätzliche Information wird dann mit den konventionellen Methoden kombiniert. Die effektive Effizienz konnte dadurch um etwa 0.3 % gesteigert werden.

Contents

| | |
|--|-----------|
| Contents | iv |
| 1. Introduction | 1 |
| 2. Experimental Setup of Belle II | 3 |
| 2.1. SuperKEKB | 3 |
| 2.2. Belle II Detector | 5 |
| 2.2.1. PXD | 5 |
| 2.2.2. SVD | 6 |
| 2.2.3. CDC | 6 |
| 2.2.4. PID | 7 |
| 2.2.5. ECL | 8 |
| 2.2.6. KLM | 9 |
| 3. Theory | 11 |
| 3.1. Introduction | 11 |
| 3.2. CKM Matrix | 12 |
| 3.3. Mixing and CP Violation | 13 |
| 3.3.1. Neutral Meson Mixing | 13 |
| 3.3.2. CP Violation in Decay | 15 |
| 3.3.3. CP Violation in Mixing | 16 |
| 3.3.4. Mixing-Induced CP Violation | 16 |
| 4. Flavor Tagging | 17 |
| 4.1. Flavor Identifying Tracks | 18 |
| 4.1.1. Leptons | 19 |
| 4.1.2. Pions | 20 |

| | |
|---|-----------|
| 4.1.3. Kaons | 21 |
| 4.1.4. Lambdas | 22 |
| 5. Multivariate Analysis | 23 |
| 5.1. Classification Problems | 23 |
| 5.2. Boosted Decision Trees | 24 |
| 5.2.1. Tree Structure | 24 |
| 5.2.2. Boosting | 25 |
| 5.3. Data Samples | 27 |
| 6. Implementation and Results | 29 |
| 6.1. Track Level | 29 |
| 6.2. Event Level | 30 |
| 6.3. Performance Measurement | 34 |
| 6.4. Integration of the Full Event Interpretation | 37 |
| 7. Conclusion | 41 |
| A. Training Variables | 43 |
| B. Decay Channels of the Full Event Interpretation | 51 |
| Bibliography | 55 |
| List of Figures | 59 |
| List of Tables | 63 |

CHAPTER 1

Introduction

The investigation of the beauty quark allows one to test the Standard Model and to search for new physics. The Belle Experiment at KEK in Tsukuba, Japan was specially designed to study B mesons which are bound states of a b and a u, d or s quark. The KEKB accelerator collided electron and positron bunches mainly at the $\Upsilon(4S)$ resonance and produced very clean samples of B meson pairs at the interaction point. At the end of the experiment in 2010 a total integrated luminosity of more than 1 ab^{-1} was reached.

A major success of the experiment was the measurement of direct and mixing-induced CP violation in several decay modes [1, 2]. Finally, the Nobel Prize was awarded in 2008 to Kobayashi and Maskawa for their theoretical work on CP violation [3]. Many other achievements have been reported, such as the observation of $B^+ \rightarrow \tau^+ \nu_\tau$ [4], the evidence for D^0 mixing [5], and the discovery of the $X(3872)$ resonance [6].

The upcoming Belle II Experiment will allow for a deeper search for new physics processes. It is envisaged to reach an instantaneous luminosity 40 times higher than its predecessor. Subsequently, the accelerator and the detector are being upgraded to cope with the new requirements and are expected to take data in 2018. Along with the hardware upgrade, most of the software tools for physics analyses are being rewritten from scratch.

The measurement of mixing-induced CP violation in the ‘Golden Mode’ $B^0 \rightarrow J/\Psi K_S^0$ will be one of the first analyses. Here, one neutral B meson decays to a CP eigenstate which is flavor-unspecific. Nevertheless, knowledge about the flavor is necessary for the measurement and can be extracted by a technique called Flavor Tagging. In this work the implementation of Flavor Tagging for the Belle II Experiment is presented.

CHAPTER 2

Experimental Setup of Belle II

The great experimental successes of the Belle Experiment and the awarding of the Noble Prize to Kobayashi and Maskawa in 2008 for their theoretical work led to the decision to upgrade the experiment. The Belle II Experiment is located at the same spot as its predecessor. The main objective is to increase the luminosity by a factor of 40 to $\mathcal{L} = 8 \times 10^{35} \text{ cm}^{-2} \text{ s}^{-1}$. Although many components can be reused, several parts of the detector and accelerator have to be upgraded. In the following section an overview of the main components will be given, following the technical design report of the Belle II Experiment [9].

2.1

SuperKEKB

The SuperKEKB accelerator is an asymmetric electron-positron collider operating at the $\Upsilon(4S)$ resonance. Electron and positron bunches with energies of 7 GeV and 4 GeV, respectively, are collided with a small angle at the interaction point, leading to a center-of-mass energy of

$$\begin{aligned}\sqrt{s} &= \sqrt{(\mathbf{P}_{e^-} + \mathbf{P}_{e^+})^2} \\ &= \sqrt{2m_{e^-}^2 c^4 + 2E_{e^-}E_{e^+} + 2|\vec{p}_{e^-}||\vec{p}_{e^+}|} \\ &= \sqrt{4E_{e^-}E_{e^+}} \\ &= 10.58 \text{ GeV}.\end{aligned}\tag{2.1}$$

Low-emittance electrons are produced at the pre-injector by a short-pulsed laser shooting at a cold cathode. The electrons are then accelerated up to 7 GeV

in a linear accelerator (Linac) and injected into the so-called high energy ring (HER). Positrons are generated at a tungsten target by irradiating them with electrons. Such secondary positrons have an emittance which is far too high for the required setup. Therefore, they are injected into a damping ring which reduces the emittance by a factor of 130, before they are finally accelerated to an energy of 4 GeV in the Linac and injected into the low energy ring (LER). The asymmetric beam energies lead to a Lorentz boost in the $\Upsilon(4S)$ center-of-mass system of

$$\beta_\gamma = 0.28. \quad (2.2)$$

This boost allows for a separate measurement of decaying B meson vertices. To

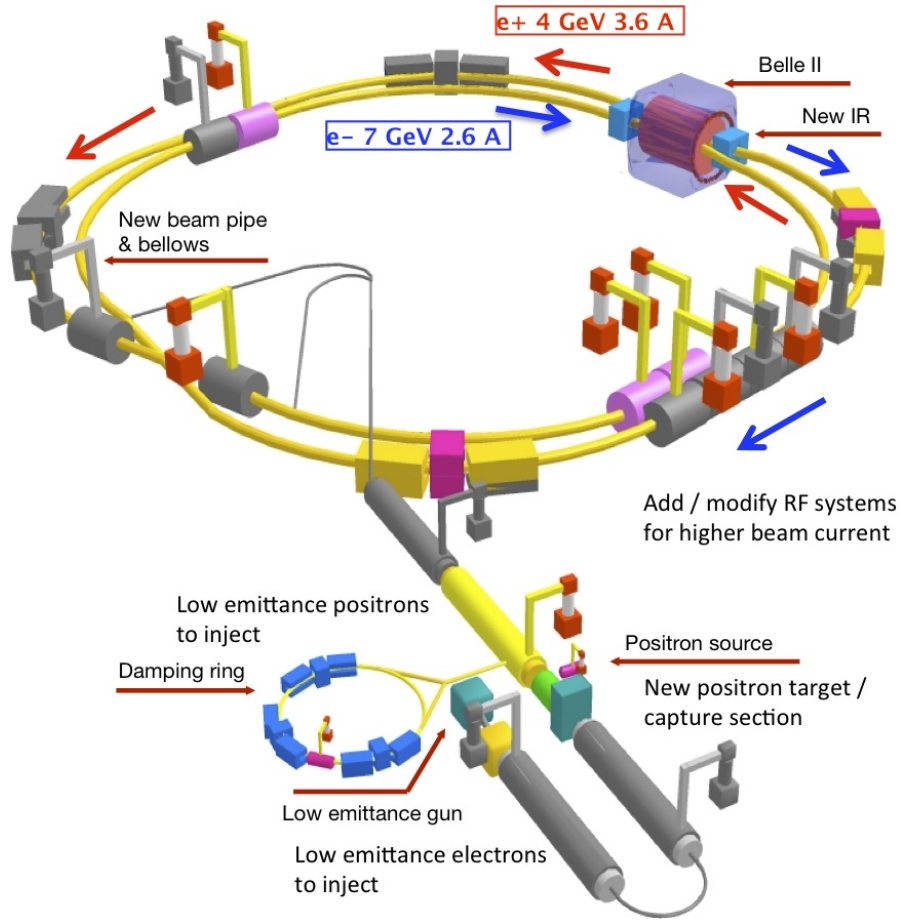


Figure 2.1.: Scheme of the SuperKEKB accelerator. The lower part shows the Linac which injects electrons and positrons into the HER, LER respectively. The beams collide at the interaction point in the Belle II detector with a center-of-mass energy of $\sqrt{s} = 10.58$ GeV. Taken from [10].

achieve the overall aim of a higher luminosity, the high current operating mode

Table 2.1.: Comparison of machine parameters between KEKB and SuperKEKB. Taken from [9].

| | KEKB | SuperKEKB |
|---|-------------|-------------|
| Energy (GeV) (e^+/e^-) | 3.5/8.0 | 4.0/7.0 |
| Beta function β_y^* | 0.129/0.090 | 0.090/0.088 |
| Current I (A) | 5.9/5.9 | 0.27/0.41 |
| Luminosity \mathcal{L} ($10^{34} \text{ cm}^{-2}\text{s}^{-1}$) | 2.11 | 80 |

used at Belle had to be dropped. Using the original setup would have led to high background rates and further technical issues. Therefore, the nano-beam scheme was adopted which enables the vertical beta function β_y^* to be reduced by a factor of 20 at the interaction point. Together with the doubled beam currents, the desired luminosity can be achieved. On the other hand, using this scheme requires that the final focus quadrupole magnets are closely positioned to the interaction point. Hence, the crossing angle had to be enlarged by a factor of 4. A readjustment of the beam energies was also necessary in order to reduce emittance. The major changes in machine parameters between SuperKEKB and its predecessor KEKB can be found in Tab. 2.1.

2.2

Belle II Detector

The design of the Belle II detector is strongly adapted from the former Belle detector. Many parts are reused, but some parts have to be upgraded to cope with the 40 times higher luminosity. Major changes came with the adaption to the nano-beam scheme. It is envisaged to perform at least as well as the Belle detector or even better.

2.2.1

PXD

The innermost part of the detector serves for the identification of the two B meson vertices. Due to the nano-beam scheme, the beam pipe radius has been reduced down to 10 mm which allows a close positioning of the PXD to the interaction point. At Belle, vertex measurements were performed by a silicon vertex detector, consisting of several silicon stripes. The higher luminosity and increasing radiation closer to the interaction point makes silicon stripes insufficient because of their increased occupancy.

Hence, a pixel detector (PXD) is used for the inner part of the vertex detector.

It is build from two layers of panels around the interaction point with depleted field effect transistors (DEPFET)[11]. The sensor enables the detection and signal amplification in the same device. The major advantages are a reduced thickness of only $75\text{ }\mu\text{m}$, air cooling and readout electronics which can be placed outside the active region and therefore reduce multiple scattering. The design of the PXD can be seen in Fig. 2.2.

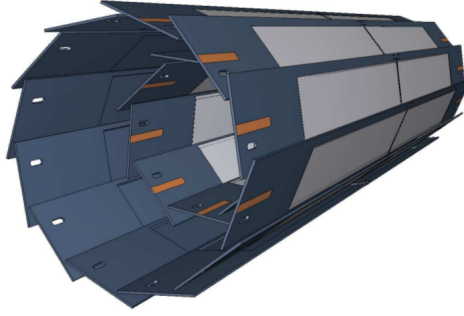


Figure 2.2.: Model of the PXD which is placed next to the interaction point. Its innermost layer has a radius of 14 mm, the outer layer one of 22 mm, respectively. [9].

2.2.2

SVD

The second part of the vertex detector consists of a silicon vertex detector (SVD). Besides the vertex measurement, low momentum tracks like slow pions with a few MeV momentum can be found, even without information from the central drift chamber. It also enables the detection of decaying K_S^0 and, with information from the SVD, tracks in the central drift chamber can be traced down to measured vertices in the PXD.

The SVD is built up of double-sided silicon strip detectors (DSSDs), arranged in four layers, around the PXD with an outer radius of 140 mm. The coverage of the polar acceptance angle is between 17° and 150° which covers for boosted B meson pairs. For the forward region slanted wafers are used. Despite a 30 times higher background rate and a smaller Lorentz boost factor leading to less B vertex separation, the combination of PXD and SVD will be as good as the vertexing at Belle.

2.2.3

CDC

The central drift chamber (CDC) extracts information about the trajectory of charged particles by measuring ionization in its gas volume. Its first objective is the reconstruction of charged tracks and the measurement of their momenta. Secondly, different particle types can be identified by their specific energy loss while crossing the CDC. Finally, trigger signals for charged tracks are generated,

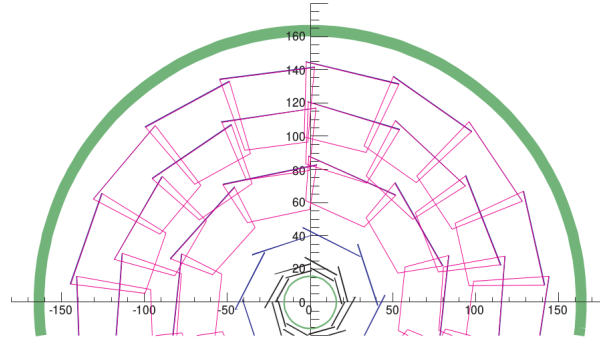


Figure 2.3.: Scheme of the SVD with its four layers of double-sided silicon strip detectors and the beampipe with PXD in the middle. Taken from [9].

where a special z-trigger signal reduces the beam background. In principle, the

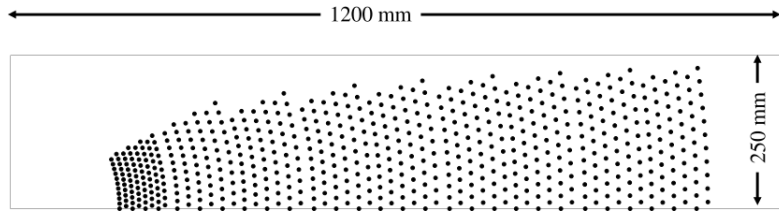


Figure 2.4.: Scheme of the CDC with its nine superlayers containing six layers. The two innermost layers serve as guards for the high background. Taken from [9].

new CDC follows the Belle design, with some upgrades like faster electronics to cope with higher trigger rates. It is constructed from 14,336 sensor wires with a diameter of $30\ \mu\text{m}$. These wires are organized in 9 superlayers, each consisting of 6 layers. The innermost layer has two additional layers as active guard wires. To determine the position of a track in z-direction, the superlayers have alternating stereo and axial orientation. The gas mixture consists of helium and ethene in equal parts.

2.2.4

PID

Particle identification is performed at the barrel and the forward endcap of the detector by a time-of-propagation counter (TOP) and an aerogel ring-imaging Cherenkov detector (ARICH), respectively.

The TOP consists of 16 modules with synthetic fused silica radiator bars. At the end a photo-detector is placed which performs the timing measurement. It replaces the former time-of-flight and aerogel Cherenkov counters of the Belle Experiment and will improve the separation power between kaons and pions.

Charged particles emit, depending on their velocity, Cherenkov photons when crossing the radiator material. These photons are emitted with a specific angle θ_c

which leads to a different time of flight for the photons through internal reflections until the bar end is reached.

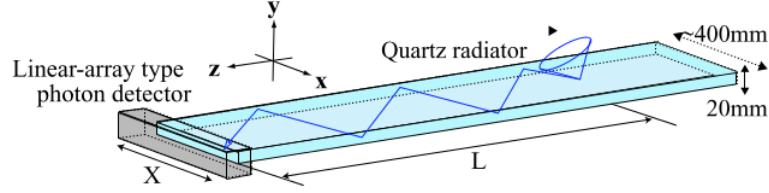


Figure 2.5.: Picture of a time-of-propagation detector bar. Pions and Kaons emit Cherenkov photons within cones of different angles which gives a distinction. Taken from [9].

The ARICH allows for kaon and pion separation up to 4 GeV. Furthermore, it gives information for the distinction of pions, muons and electrons below the 1 GeV threshold. Cherenkov photons are emitted in an aerogel medium. In a volume the rising Cherenkov cones can grow and are then finally detected by photon detectors which measure the radius of the ring.

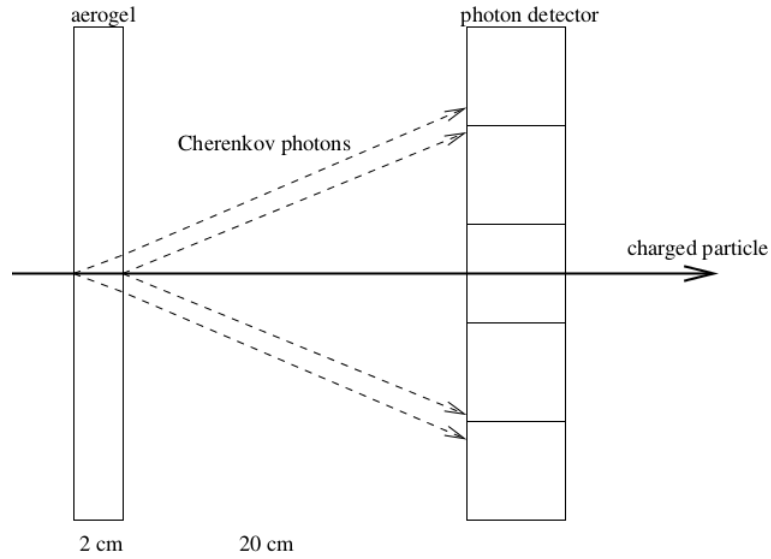


Figure 2.6.: Schematic view of the ARICH. Charged particles emit photons in the aerogel medium which propagate through a volume to a photon detector. Taken from [9].

2.2.5

ECL

The electromagnetic calorimeter (ECL) detects photons and measures their energy and angular position. Furthermore, electrons and K_L (together with the KLM) can be identified. A reliable trigger signal is produced and the luminosity measurement

can be performed. For Belle II most parts of the predecessor ECL can be reused, but have to be modified for the higher luminosity. The ECL is about 3 m long and wrapped around the interaction point with an inner radius of 1.2 m. Additionally, it has a forward and backward endcap and consists in total of 8736 CsI(Tl) scintillation crystals which weigh in total 43 tons. The scintillation readout is done by photodiodes at the end of each crystal.

With a higher luminosity several problems occur like the degradation of crystals due to higher radiation, dark current in photodiodes caused by neutron flux, pile-up noise from soft background photons and fake clusters caused by high energy background photons. In order to cope with these upcoming problems, the readout electronics were upgraded. In addition, it is thought of replacing the CsI(Tl) crystals at the endcaps by pure CsI crystals [12].

2.2.6

KLM

The K_L and muon detection is performed by the KLM. It is placed outside the superconducting solenoid and consists of iron plates and active detector parts. At the barrel it is composed of 14 iron plates and 15 detector plates, at the endcaps there are 14 iron plates and detector plates. The entire KLM offers 3.9 interaction lengths for K_L for hadronic showering. The active parts of the detector consist of glass-electrode-resistive plate chambers (RPCs) which enables the detection of charged particles from the hadronic shower in the gaps. For muon identification charged tracks are extrapolated from the CDC to the KLM and are accepted if there are associated hits. For K_L identification, hits are grouped into clusters and aligned with neutral ECL clusters which gives better positional information. Fluctuations in the shower development give no reliable statement on the energy deposition.

Due to the high background rates with a larger luminosity, the RPCs at the endcaps will be replaced by scintillator stripes. The scintillation light will be forwarded to a silicon photo multiplier by wavelength-shifting fibers.

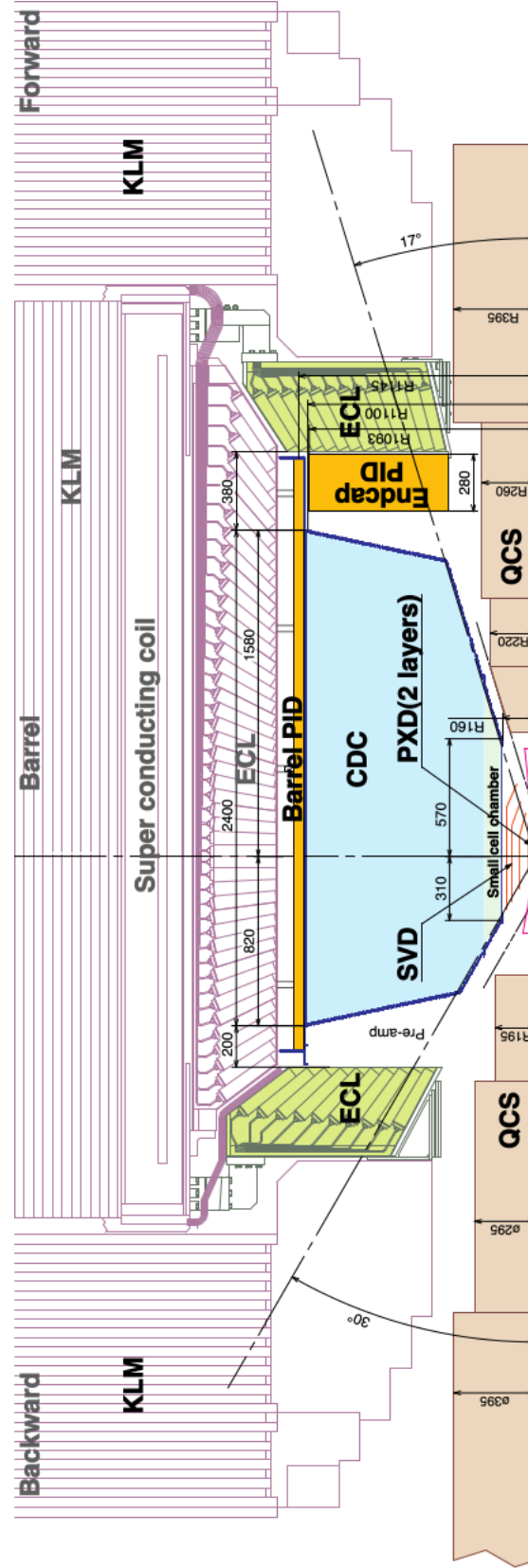


Figure 2.7.: Cut through the Belle II detector. The interaction point in the middle is surrounded by the PXD and SVD for a close vertex measurement, surrounded by the CDC for track reconstruction. It is followed by the PID and ECL. The outermost part for K_L and muon identification is given by the KLM. Taken from [9].

CHAPTER 3

Theory

3.1

Introduction

The Standard Model of particle physics can be described mathematically as a gauge theory

$$SU(3)_C \times SU(2)_L \times U(1)_Y, \quad (3.1)$$

where the electroweak sector is represented by the $SU(2)_L \times U(1)_Y$ symmetry and the strong sector by $SU(3)_C$. The theory describes the constituents of matter and the interactions between them, except for the gravitational force.

Matter consists of fermions which have half integer spin and can be grouped into three generations of either leptons or quarks. Each charged lepton has an uncharged neutrino partner. The three quark generations consist of an up-type and a down-type like quark with charges of $+2/3e$ and $-1/3e$, respectively. The quark masses differ in a wide range between a few MeV up to the GeV scale. Due to color confinement, quarks can only be found in bound color neutral states, either as a baryon consisting of three quarks (anti-quarks) or as a meson consisting of a quark anti-quark pair.

Interactions are mediated by gauge bosons with integer spin. The photon γ carries the electromagnetic force between charged particles, the W^\pm and Z bosons mediate the weak interaction of leptons and quarks. The strong interaction between quarks is represented by eight gluons. The recently found Higgs boson completes the Standard Model. It mediates the Higgs field and thereby generates the mass of fermions.

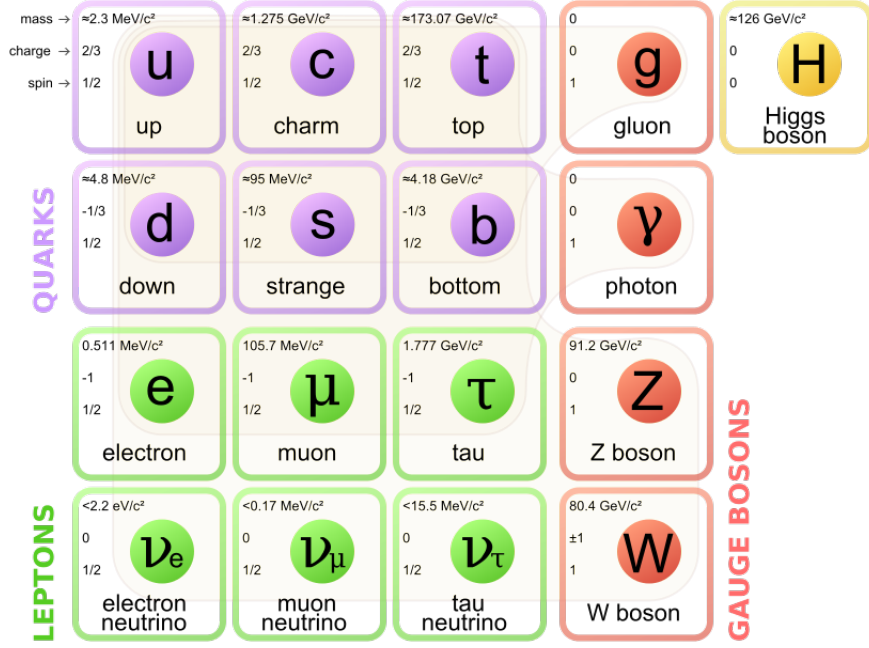


Figure 3.1.: Overview of the Standard Model with its three generations of fermions, the gauge and Higgs bosons. Taken from [13].

3.2

CKM Matrix

Flavor changing transitions between quarks are mediated by charged currents of the weak interaction. Besides transitions within a generation, transitions between generations are also allowed to a small degree. To explain the different coupling of the weak interaction, Cabibbo introduced a (2×2) quark matrix with a mixing angle θ_C [14]. The Cabibbo angle rotates the mass eigenstates to weak eigenstates

$$\begin{aligned} |d'\rangle &= \cos \theta_C |d\rangle + \sin \theta_C |s\rangle, \\ |s'\rangle &= \cos \theta_C |s\rangle - \sin \theta_C |d\rangle. \end{aligned} \quad (3.2)$$

Later on, Kobayashi and Maskawa extended the concept by establishing a unitary (3×3) matrix in order to explain CP violation [15]

$$V_{CKM} = \begin{pmatrix} V_{ud} & V_{us} & V_{ub} \\ V_{cd} & V_{cs} & V_{cb} \\ V_{td} & V_{ts} & V_{tb} \end{pmatrix}. \quad (3.3)$$

Thereby, they added a so far unknown third quark generation to the Standard Model. The Cabibbo-Kobayashi-Maskawa (CKM) matrix possesses four free

(physical) parameters: three mixing angles and one irreducible complex phase, which allows CP violation. The Wolfenstein parametrization offers a deeper understanding of the hierarchy

$$V_{CKM} = \begin{pmatrix} 1 - \lambda^2/2 & \lambda & A\lambda^3(\rho - i\eta) \\ -\lambda & 1 - \lambda^2/2 & A\lambda^2 \\ A\lambda^3(1 - \rho - i\eta) & -A\lambda^2 & 1 \end{pmatrix} + O(\lambda^4), \quad (3.4)$$

with the real parameters A , ρ and η and the element $\lambda \approx 0.22$ [16]. Transitions within a generation, represented by diagonal elements are hardly suppressed. Whereas the elements V_{ub} and V_{td} suffer under a high suppression of λ^3 .

The CKM elements can be visualized in a complex plane by using the unitary condition $V_{CKM}V_{CKM}^\dagger = V_{CKM}^\dagger V_{CKM} = 1$. For the most interesting elements one obtains the following relation

$$V_{ud}V_{ub}^* + V_{cd}V_{cb}^* + V_{td}V_{tb}^* = 0. \quad (3.5)$$

The equation can be visualized by a unitary triangle under the approximations of

$$\bar{\rho} = \rho(1 - \lambda^2/2), \quad \bar{\eta} = \eta(1 - \lambda^2/2). \quad (3.6)$$

It is normalized by a factor of $|V_{cd}V_{cb}^*|$ and has an apex at $(\bar{\rho}, \bar{\eta})$. The angles are defined as

$$\alpha = \arg\left(-\frac{V_{td}V_{tb}^*}{V_{ud}V_{ub}^*}\right) \quad \beta = \arg\left(-\frac{V_{cd}V_{cb}^*}{V_{td}V_{tb}^*}\right) \quad \gamma = \arg\left(-\frac{V_{ud}V_{ub}^*}{V_{cd}V_{cb}^*}\right) \quad (3.7)$$

An overview of the measurements of $\bar{\rho}$ and $\bar{\eta}$ can be seen in Fig. 3.2.

3.3

Mixing and CP Violation

This section gives a short overview of phenomena linked to neutral mesons. For a complete discussion the reader is referred to [18].

3.3.1

Neutral Meson Mixing

An interesting fact of neutral mesons is mixing, i.e., the oscillation of a meson to its anti-meson and vice versa. It is based on the incompatibility of mass ($|M_L\rangle$, $|M_H\rangle$) and flavor eigenstates ($|M^0\rangle$, $|\bar{M}^0\rangle$). A meson state can be described as a superposition of flavor eigenstates. At the time $t = 0$ it can be written as

$$|\Psi(0)\rangle = a(0)|M^0\rangle + b(0)|\bar{M}^0\rangle. \quad (3.8)$$

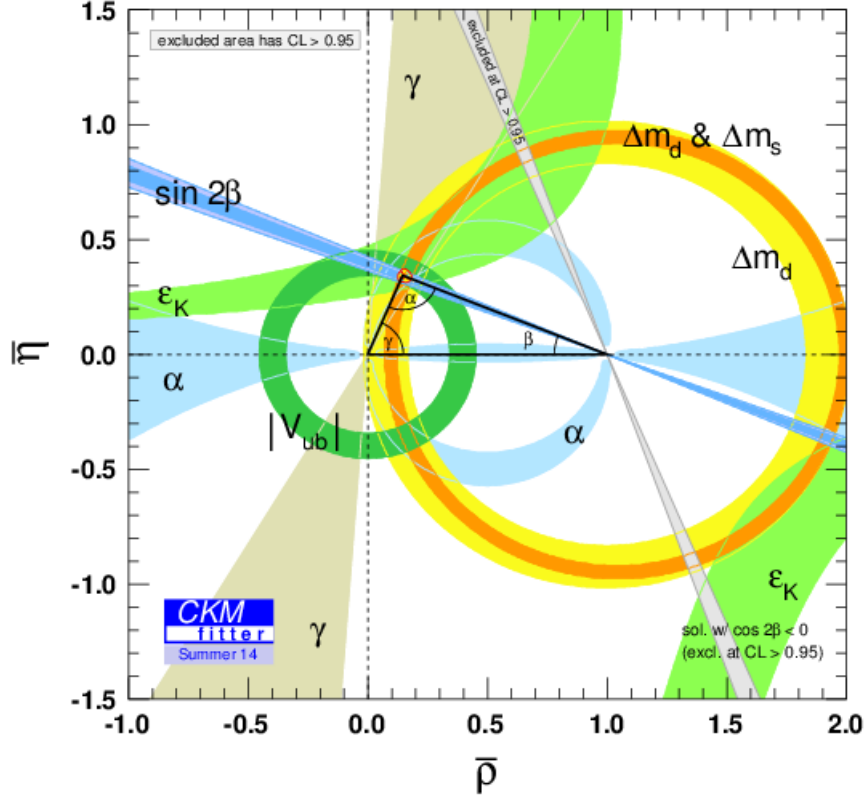


Figure 3.2.: Actual constraints for the measurement of $\bar{\rho}$ and $\bar{\eta}$ [17].

The state evolves in time and additional final states have to be considered due to decay

$$|\Psi(t)\rangle = a(t)|M^0\rangle + b(t)|\bar{M}^0\rangle + c_1(t)|f_1\rangle + c_2(t)|f_2\rangle + \dots \quad (3.9)$$

It can be approximated and written into a time-dependent Schrödinger equation with a non-hermitian Hamiltonian \mathcal{H}_{eff} . This Hamiltonian can be split into a mass and a decay matrix

$$\mathcal{H}_{eff} = \begin{pmatrix} M_{11} & M_{12} \\ M_{12}^* & M_{22} \end{pmatrix} - \frac{i}{2} \begin{pmatrix} \Gamma_{11} & \Gamma_{12} \\ \Gamma_{12}^* & \Gamma_{22} \end{pmatrix}, \quad (3.10)$$

where the diagonal elements of these (2×2) matrices are responsible for flavor-conserving transitions. The off-diagonal elements are flavor changing. In addition,

the mass eigenstates of the effective Hamiltonian can be written as

$$\begin{aligned} |M_L\rangle &= p|M^0\rangle + q|\bar{M}^0\rangle, \\ |M_H\rangle &= p|M^0\rangle - q|\bar{M}^0\rangle, \end{aligned} \quad (3.11)$$

where q and p denote complex coefficients with $|p|^2 + |q|^2 = 1$. The mass and lifetime differences of the two states are gives by

$$\begin{aligned} \Delta m &= \text{Re}(\lambda_H - \lambda_L), \\ \Delta\Gamma &= 2\text{Im}(\lambda_H - \lambda_L), \end{aligned} \quad (3.12)$$

where $\lambda_{L,H}$ denotes the eigenvalues of \mathcal{H}_{eff} .

3.3.2

CP Violation in Decay

The first type of CP violation is not related to meson oscillations and can happen in neutral and charged decays. It occurs, when the decay rate of a meson M to a final state f differs from the decay rate of the anti-meson \bar{M}

$$\Gamma(M \rightarrow f) \neq \Gamma(\bar{M} \rightarrow \bar{f}). \quad (3.13)$$

This can only be established if two or more diagrams are involved in a process. The resulting amplitude for a meson is given by

$$A_f = |a_1|e^{i(\delta_1+\phi_1)} + |a_2|e^{i(\delta_2+\phi_2)}, \quad (3.14)$$

and its CP conjugated counterpart is given by

$$\bar{A}_{\bar{f}} = |a_1|e^{i(\delta_1-\phi_1)} + |a_2|e^{i(\delta_2-\phi_2)}, \quad (3.15)$$

where a_i is the amplitude, ϕ_i the CP violating phase and δ_i a strong CP conserving phase appearing through hadronic interactions. CP violation is established if the absolute value of the amplitudes differ, i.e.,

$$\left| \frac{\bar{A}_{\bar{f}}}{A_f} \right| \neq 1. \quad (3.16)$$

The first experimental proof of CP violation in decay for the B meson system was found in the mode $B^0 \rightarrow K^+\pi^-$ by the BABAR experiment in 2004 [19].

3.3.3

CP Violation in Mixing

The second type of CP violation is closely related to mixing in neutral meson systems. It occurs, when the oscillation of a meson to the anti-meson is unequal to the oscillation in the opposite direction

$$\Gamma(M^0 \rightarrow \bar{M}^0) \neq \Gamma(\bar{M}^0 \rightarrow M^0). \quad (3.17)$$

The condition can be written as

$$|p| \neq |q|. \quad (3.18)$$

This type of CP violation is usually measured in semileptonic decays.

3.3.4

Mixing-Induced CP Violation

Mixing-induced CP violation can take place in a meson system even if there is no violation in decay or mixing. It is possible through the interference of decays with and without mixing. One meson decays to a final CP eigenstate $M^0 \rightarrow f_{CP}$ and the other decays to the same final state but with additional mixing $M^0 \rightarrow \bar{M}^0 \rightarrow f_{CP}$. It occurs if the following condition is satisfied

$$\text{Im}(\lambda_f) \neq 0, \quad (3.19)$$

where

$$\lambda_f = \frac{q}{p} \frac{\bar{A}_f}{A_f}. \quad (3.20)$$

Experimentally, the asymmetry is given as

$$\mathcal{A}_{f_{CP}} = \frac{\Gamma(\bar{M}^0(\Delta t) \rightarrow f_{CP}) - \Gamma(M^0(\Delta t) \rightarrow f_{CP})}{\Gamma(\bar{M}^0(\Delta t) \rightarrow f_{CP}) + \Gamma(M^0(\Delta t) \rightarrow f_{CP})}, \quad (3.21)$$

where Δt denotes the difference in decay times between the both mesons in the event.

In the case of neutral B mesons where CP violation in decay and CP violation in mixing can be neglected the equation reduces to

$$\mathcal{A}_{f_{CP}} = S_{f_{CP}} \sin \Delta m \Delta t, \quad (3.22)$$

where $S_{f_{CP}}$ is obtained by fitting the Δt distribution. This has been precisely measured, e.g., in the ‘Golden Mode’ $B^0 \rightarrow J/\Psi K_S^0$ [20, 21].

CHAPTER 4

Flavor Tagging

The next generation B -Factory will produce large amounts of B mesons. The produced $\Upsilon(4S)$ resonance decays almost exclusively into an entangled neutral or charged B meson pair, nearly in equal parts. Neutral B meson systems are of interest in the investigation of mixing-induced CP violation. Once one meson decays to a flavor-specific final state, the flavor is fixed for both. In the measurement

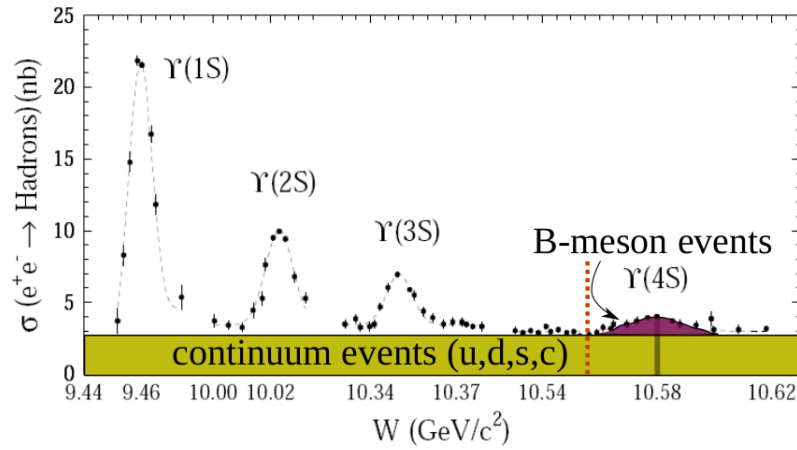


Figure 4.1.: Production of B meson pairs at the $\Upsilon(4S)$ resonance. Taken from [22].

of mixing-induced CP violation one meson is reconstructed in a flavor unspecific CP eigenstate, see Eq. 3.21. Furthermore, the decay time difference Δt between both B mesons has to be measured as

$$\Delta t = \frac{\Delta z}{\beta_\gamma c}, \quad (4.1)$$

where Δz denotes the difference of decay lengths along the z-axis and β_γ describes the boost. In addition, knowledge about the flavor at the time of decay is crucial, which is the final goal of a Flavor Tagging algorithm.

Particles from which the CP eigenstate is reconstructed are assigned to the

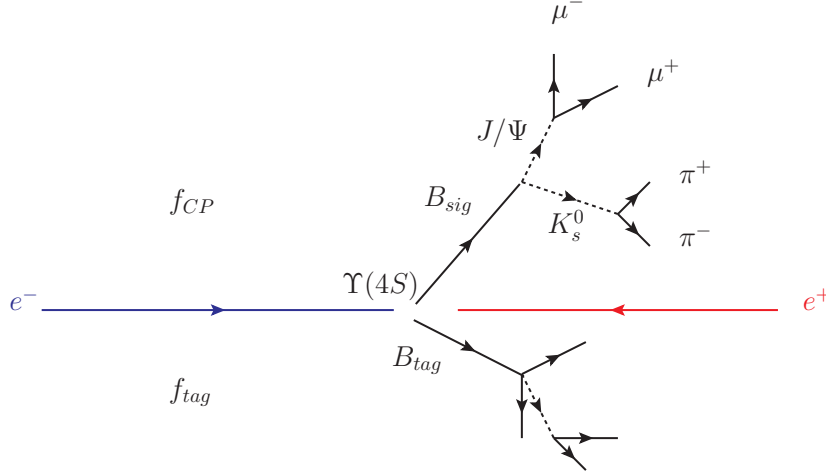


Figure 4.2.: Reconstruction of the CP eigenstate on the signal-side f_{CP} , the tracks on the tag-side f_{tag} are used for Flavor Tagging.

signal-side f_{CP} of the event (Fig. 4.2). All remaining particles originate from the second B meson on the so-called tag-side f_{tag} . Due to the entangled state of the B pair, the knowledge of the tag-side flavor automatically determines the signal-side flavor.

4.1

Flavor Identifying Tracks

Some final states of decaying B mesons imply flavor information. In the following, such final states are specified. However, it is not always feasible to deduce flavor information, since many decay modes reveal none or very little information [7]. For example, decays with uncharged final state particles such as

$$\begin{aligned} B^0 &\rightarrow \bar{D}^0 \pi^0 \\ &\rightarrow K^0 \pi^0. \end{aligned} \tag{4.2}$$

The performance of Flavor Tagging strongly depends on the detector efficiency. It can also be decreased by misidentified particles, as well as modes with opposite charged final state particles compared to the major processes. Due to a wide range of decay modes, inclusive methods are used.

4.1.1

Leptons

Primary leptons originate directly from B mesons in semileptonic decays. These modes are due to leading order weak interaction mediated by a charged W^\pm boson. The charge of direct leptons is associated with the flavor of its mother particle

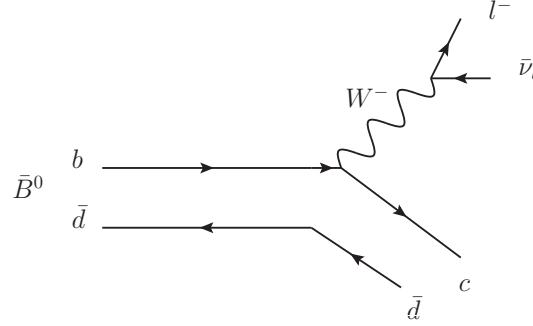


Figure 4.3.: Production process for direct leptons.

(Fig. 4.3). In a $b \rightarrow cl^- \bar{\nu}_l$ semileptonic decay a positively (negatively) charged lepton indicates a B^0 (\bar{B}^0) decay

$$\bar{B}^0 \rightarrow Xl^- \bar{\nu}_l, \quad (4.3)$$

where X indicates another hadronic particle.

Secondary leptons descend from semileptonic decaying D mesons via $b \rightarrow c \rightarrow s$ transitions. In this cascade decay the charge of the lepton corresponding to the B meson is reversed: a negatively (positively) charged lepton indicates a B^0 (\bar{B}^0)

$$\bar{B}^0 \rightarrow DX \rightarrow X'l^+ \nu_l. \quad (4.4)$$

Many variables can be used for the identification of the lepton candidates such as the the charge or particle identification probability (PID). Kinematic variables including the momentum in the center-of-mass frame p_{cms} allow a good separation, especially for the identification of a direct lepton. On the other hand, a lepton originating from a D decay does not have a high momentum, as there was a lot of energy already absorbed by the mother D meson, therefore a softer momentum spectrum is expected. The distribution of the momentum and the angle between the missing momentum and the lepton on Monte Carlo can be seen in Fig. 4.4. Moreover, variables like the missing momentum in the $\Upsilon(4S)$ frame p_{miss} or the mass recoiling against the missing and lepton momentum M_{recoil} enable a further separation.

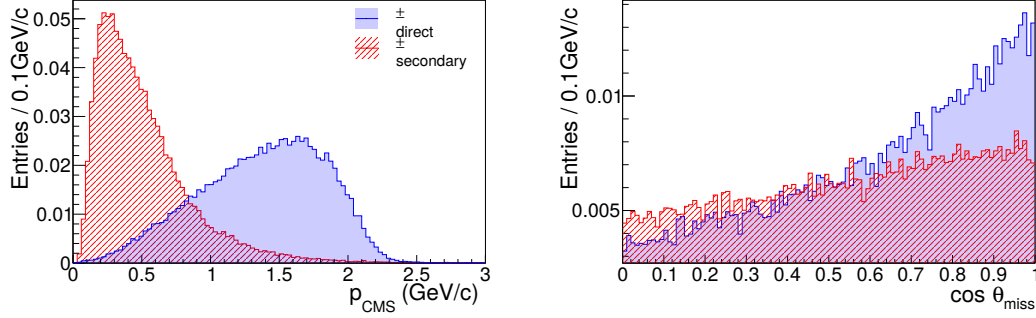


Figure 4.4.: Distribution of p_{cms} (left) and $\cos\theta_{miss}$ (right) for direct (solid) and secondary (hashed) muons on Monte Carlo, see Sec. 5.3.

4.1.2

Pions

Pions are the most common final state particles. Slow pions originate from a $D^{*\pm}$ decay, where a negatively (positively) charged pion indicates a B^0 (\bar{B}^0)

$$\begin{aligned} \bar{B}^0 &\rightarrow D^{*+} X \\ &\rightarrow D^0 \pi^+. \end{aligned} \quad (4.5)$$

Because of the low mass difference between the D^{*+} and the D^0 , slow pions are produced nearly at rest in the D^{*+} frame. The pion moves nearly in the same direction as the D^0 in the B_{tag} frame. On the contrary, pions coming from the

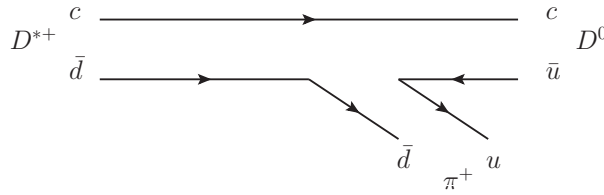


Figure 4.5.: Production process for slow pions.

hadronization of a W boson have a higher momentum, e.g., in the decay

$$\bar{B}^0 \rightarrow D^{*+} \pi^- X. \quad (4.6)$$

Besides p_{cms} and the polar angle in the lab frame θ_{lab} , the thrust angle between the remaining particles on the tag-side and the pion α_{thrust} is relevant to distinguish between fast and slow pions (Fig. 4.6).

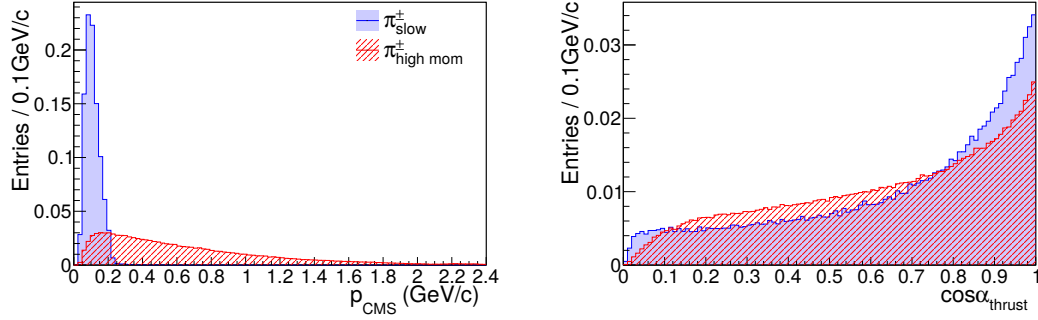


Figure 4.6.: Distribution of p_{cms} (left) and α_{thrust} (right) for slow (solid) and high momentum (hashed) pions on Monte Carlo, see Sec. 5.3.

4.1.3

Kaons

Kaons give the most powerful flavor identification and also have a high occurrence in B^0 decays. They mainly originate from $b \rightarrow c \rightarrow s$ cascade decays

$$\begin{aligned} \bar{B}^0 &\rightarrow DX \\ &\rightarrow K^- X'. \end{aligned} \quad (4.7)$$

A positively (negatively) charged kaon indicates a B^0 (\bar{B}^0), as illustrated in Fig. 4.7. Since the mother of the kaon is unclear, it can also originate from charm decay or $s\bar{s}$ quark pair popping out of the vacuum, therefore combining the total charge is important. Emerging K_S^0 can indicate a kaon from $s\bar{s}$ quark pair popping. In addition to kinematic variables like p_{cms} and θ_{lab} , the charge and PID can help to identify candidates.

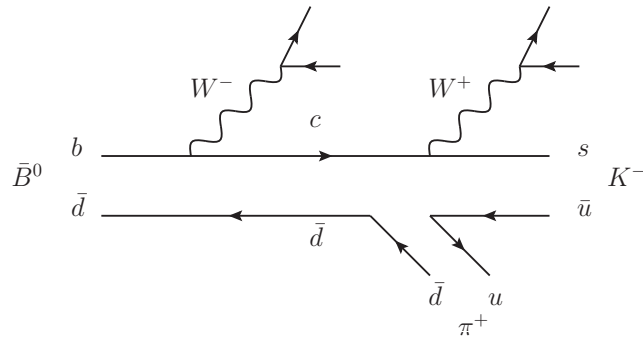


Figure 4.7.: Production process for kaons.

4.1.4

Lambdas

Lambdas are not directly measured as final state particles but have to be reconstructed from protons and pions. They can arise through a $b \rightarrow c \rightarrow s$ cascade decay, such as

$$\begin{aligned} \bar{B}^0 &\rightarrow \bar{\Lambda}_c^+ X \\ &\rightarrow \bar{\Lambda}_0 X'. \end{aligned} \quad (4.8)$$

Despite their very low occurrence in B meson events, they are valuable for flavor determination. A lambda (anti-lambda) indicates a B^0 (\bar{B}^0). The quality of a lambda candidate depends on a correct reconstruction, therefore the quality of the lambda vertex is of interest. The angle between the lambda momentum, its vertex and the interaction point θ_Λ can also give information about a good candidate, as well as its mass M_Λ .

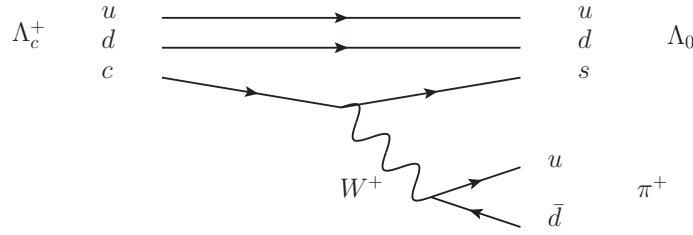


Figure 4.8.: Production process for lambdas.

CHAPTER 5

Multivariate Analysis

5.1

Classification Problems

A common task in physics analyses is the classification of data samples into subsets. In the case of Flavor Tagging, candidate tracks are assigned to different flavor-specific categories. For a plausible statement of the tag-side B meson flavor, one is interested in correctly identified tracks, e.g., slow pion tracks have to be separated from high momentum pions and other tracks, which could give wrong flavor information.

A binary classification between signal (slow pions) and background (all remaining tracks) can be done by applying a cut on an input variable, e.g., candidates with a momentum above a certain threshold are rejected as background. The performance of such a classifier depends on the harshness of the applied cuts, which influences the efficiency and the purity, defined as follows:

$$\epsilon = \frac{N(\text{selected signals})}{N(\text{signals in dataset})} \quad (5.1)$$

$$p = \frac{N(\text{selected signals})}{N(\text{selected events})} \quad (5.2)$$

Compared to a hard cut, a soft cut increases the efficiency but lowers the purity, since more signal candidates are accepted but less background candidates are rejected.

Applying cuts on candidates is not optimal because correlations between different input variables cannot be treated well. Hence, multivariate classifiers are applied which are much better suited to tackle these problems. A multivariate classifier

can be described as a function which maps the input variables of a candidate $\mathbf{x} = \{x_1, \dots, x_n\}$ onto a single discriminant h , by using weights $\mathbf{a} = \{a_1, \dots, a_n\}$

$$h = h(\mathbf{x}, \mathbf{a}). \quad (5.3)$$

The optimal weights of such a classifier have to be determined by supervised training, i.e., the classifier is trained on a data sample $\{y_i, \mathbf{x}_i\}_1^N$ of N events, where y_i represents the known truth.

The Belle II Analysis Framework (basf2) provides a package called TMVA (Toolkit for Multivariate Data Analysis) [23], which offers several multivariate analysis methods such as simple Fisher discriminant [24], NeuroBayes [25] or Boosted Decision Trees (BDT) [26]. The latter is described in the next section, since it is used for this work.

5.2

Boosted Decision Trees

5.2.1

Tree Structure

Decision Trees are based on an iterative learning process. As depicted in Fig. 5.1, a decision tree consists of different levels of binary nodes. Starting from the root node, the sample is split into two parts by using the input variable with the highest separation power. An input variable can be used several times for splitting. The whole process is repeated until a specified depth of nodes is reached.

Like other multivariate methods, decision trees can be overtrained, i.e., the clas-

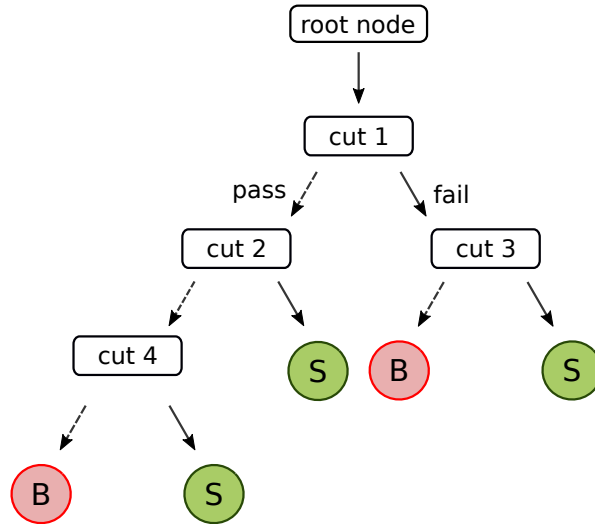


Figure 5.1.: Structure of a decision tree.

sifier learns statistical fluctuations of the data. It can be caused by a insufficiently

large training sample, a method which is too complex, or the use of too many discriminating variables. Hence, the classifier loses its separation power on an independent sample. In order to check for overtraining, TMVA splits the given sample into a training and test sample and applies a Kolmogorov-Smirnov test [27]. This is depicted in Fig. 5.3.

5.2.2

Boosting

To improve the classifier performance and to avoid overtraining, a procedure called boosting is applied. Instead of one tree, a forest of ‘weak’ trees is trained. Each tree learns only a small aspect of the data and is then combined in such a manner that a ‘strong’ classifier is obtained. The final classifier allows more stability with respect to fluctuations and a drastically improved separation power. Several boosting algorithms are available, such as Adaptive Boosting [28] or Gradient Boosting [26], which is discussed below.

A combination of weak base learners $h(x, a_m)$ to a final strong learner can be written as an additive expansion

$$H(x) = \sum_{m=0}^M \beta_m h(x, a_m), \quad (5.4)$$

where β_m represents the expansion coefficient. To achieve an optimal classifier, a loss function has to be minimized. Since the minimization of the loss function is not trivial, the weights are determined in an iterative processes where in each step the gradient of the loss functions has to be calculated. Through the iteration, the decision trees are focused onto the misclassified events. Stochastic Gradient Boosting is a further improvement, where only a smaller random sample of candidates are used for training. A more detailed description of the algorithm can be found in [29].

Besides performance issues, Flavor Tagging is independent from the used multivariate classifier. In this work, an implementation of BDTs was chosen for classification problems, due to their robustness and fast implementation [8]. The method uses a Stochastic Gradient Boosting with a log likelihood loss function

$$L(H, y) = \ln(1 + e^{-2H(x)y}). \quad (5.5)$$

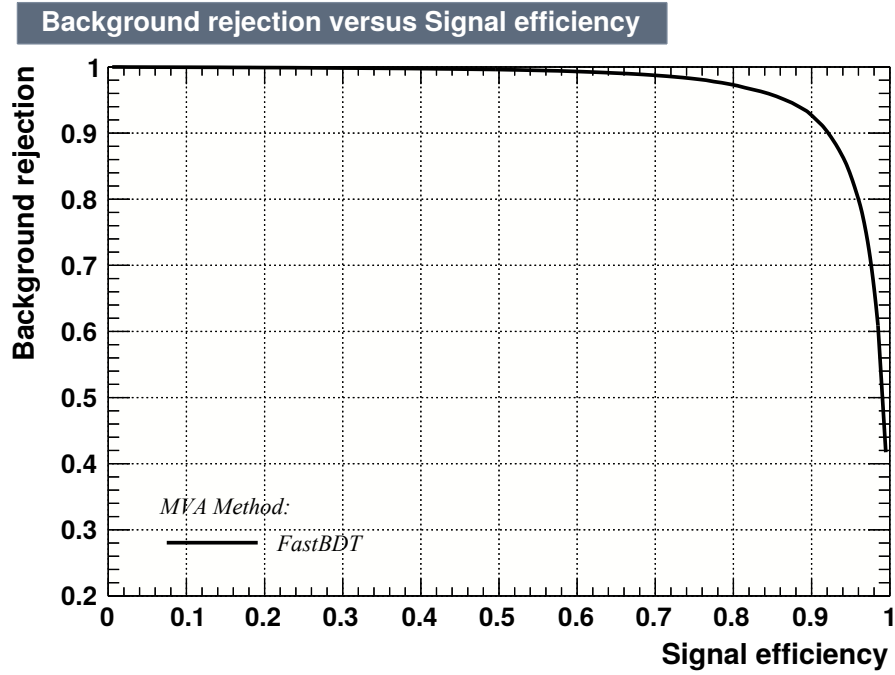


Figure 5.2.: Example of a ROC curve plot provided by TMVA. It shows signal efficiency against background rejection.

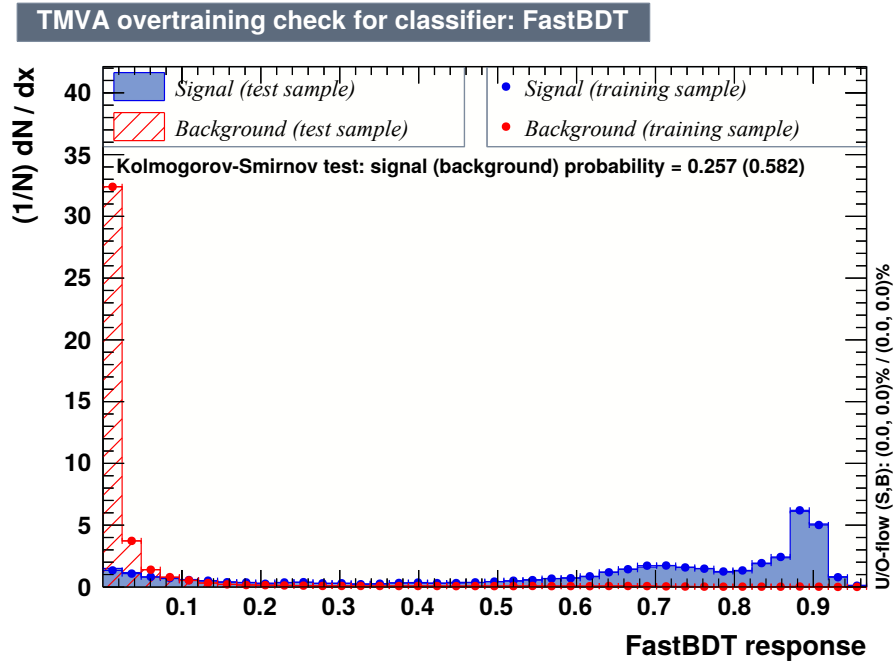


Figure 5.3.: Example of an overtraining check provided by TMVA. It shows the results for training (dots) and test sample (shaded area) for the signal and background distribution. The Kolmogorov-Smirnov test also allows to check for overtraining.

5.3

Data Samples

Multivariate classifiers are usually trained on Monte Carlo samples with known truth. The events in this work are generated with the EvtGen package [30], the detector response is simulated with the GEANT4 package [31].

Two types of a special Monte Carlo without beam background are used in Chap. 6. For Flavor Tagging only neutral B meson pairs are generated where the signal-side decays with 100% branching fraction to the CP eigenstate $J/\Psi K_S^0$. The tag-side decays generically, i.e., the B meson decays according to the PDG branching fractions [32]:

$$\begin{aligned} B_{sig} &\rightarrow J/\Psi(\rightarrow \mu^+ \mu^-) \quad K_S^0(\rightarrow \pi^+ \pi^-), \\ B_{tag} &\rightarrow \text{generic}. \end{aligned} \tag{5.6}$$

The additional classifiers of the Full Event Interpretation are trained externally on neutral B meson Monte Carlo with a signal-side which decays to non-existing decay channel $B \rightarrow \nu \bar{\nu}$. The tag-side decays generically:

$$\begin{aligned} B_{sig} &\rightarrow \nu \bar{\nu}, \\ B_{tag} &\rightarrow \text{generic}. \end{aligned} \tag{5.7}$$

This ‘mono-generic’ Monte Carlo is used to ensure that the classifiers are only trained on the signal-side.

CHAPTER 6

Implementation and Results

The implementation of Flavor Tagging is based on the approach of the Belle Experiment, which was structured into two parts [7]. Firstly, tracks were assigned to five flavor-specific categories and were evaluated according to their characteristics using multi-dimensional look-up tables. Secondly, the candidates of the categories were combined to a final result for the B meson flavor.

The design of the algorithm for Belle II was changed in some aspects and is presented in this chapter. It is shown how the performance can be measured and how it compares to the Belle Experiment. Subsequently, an extension is presented including the Full Event Interpretation [8].

6.1

Track Level

Tracks from the tag-side are analyzed at the track level. It can be assumed, that all remaining tracks originate from the tag-side B meson, if the signal-side of an event is correctly reconstructed. A typical $B^0\bar{B}^0$ event contains around 10 tracks which are selected under different (anti-)particle hypothesis: electrons, muons, pions and kaons. In addition, lambdas are reconstructed from protons and pions. An overview of these flavor-specific categories can be found in Chap. 4.

The classification for each flavor-specific category is done by multivariate methods, where each candidate is evaluated according to its input variables. The classifiers have to be trained on Monte Carlo where the full information of the event is available, see Chap. 5. They are trained in such a way that tracks which belong to the particle category and originate from the specified B decay are separated. To increase the separation power, additional input variables used by the BaBar

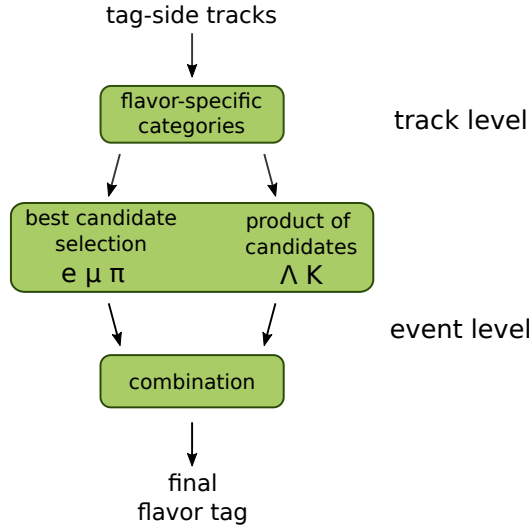


Figure 6.1.: General approach of the Flavor Tagging.

Experiment were added [33, Chap.8]. A complete list of the variables can be found in Appendix A. The output of a trained classifier, the so-called track level dilution factor r , lies in the range between 0 for a random and 1 for reliable decision. The flavor information q is extracted from the charge of the track, where $+1$ (-1) indicates a B^0 (\bar{B}^0). Both parameters are combined to the qr value, which gives the full sub-tagger information.

6.2

Event Level

The individual categories are combined at event level to return the final flavor information. Although this information can already be extracted from a sub-tagger it is reasonable to combine all information for an optimal final output.

In case of several candidates in a category, a selection has to be performed. At Belle the best candidate of all lepton categories was taken, regardless if it was a secondary or direct particle, since the number of leptons is low in most events. On the other hand, the lambda and kaon category were combined at event level by calculating a weighted product of the sub-tagger output of all candidates i

$$(qr) = \frac{\prod_i (1 + (q \cdot r)_i) - \prod_i (1 - (q \cdot r)_i)}{\prod_i (1 + (q \cdot r)_i) + \prod_i (1 - (q \cdot r)_i)}. \quad (6.1)$$

In order to use all available information for this approach, all categories are fed separately into the event level. For each lepton and pion category the best candidate is chosen, i.e., the candidate with the highest track-level dilution factor

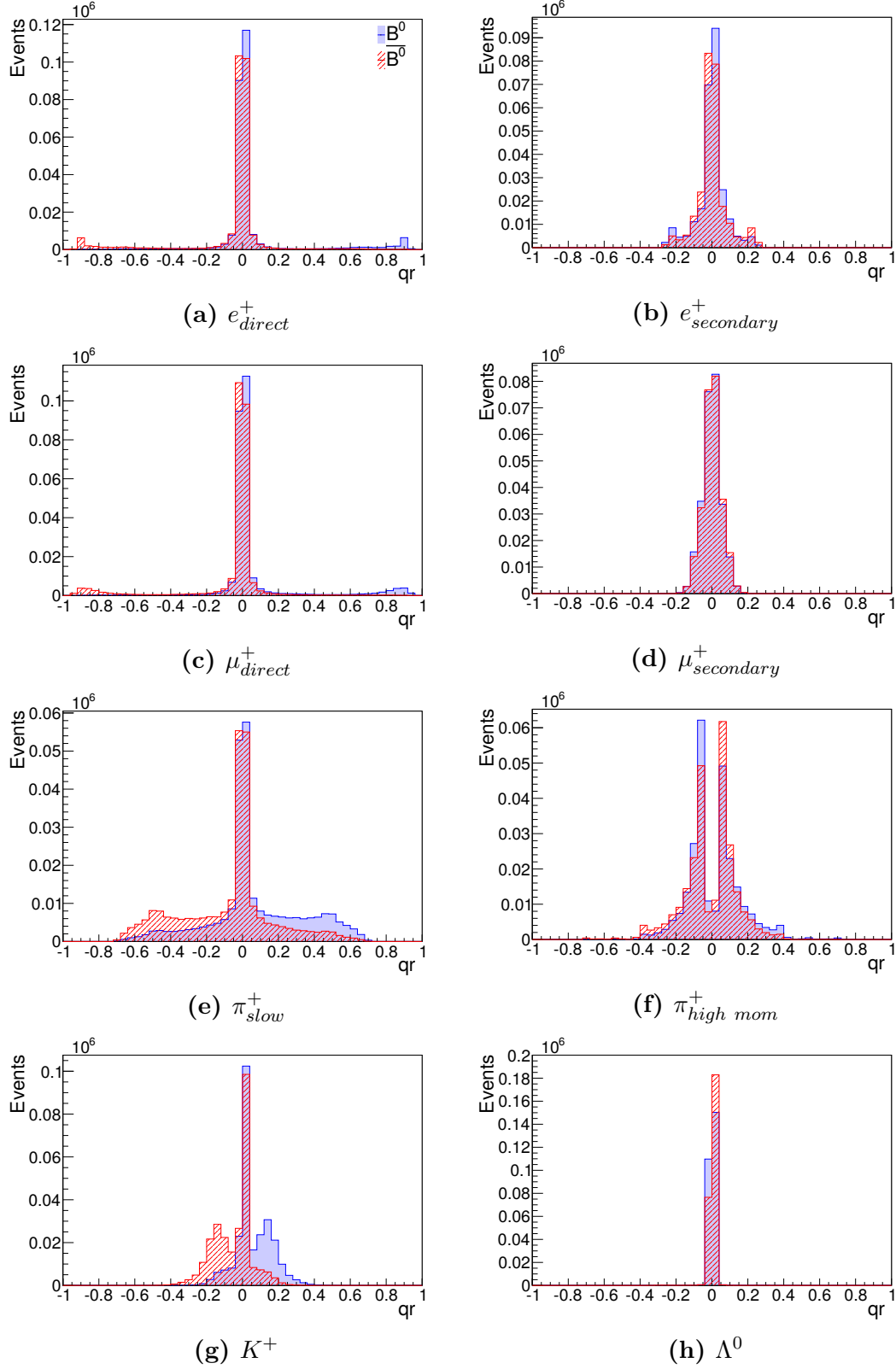


Figure 6.2.: Output of the sub-taggers for leptonic (a-d) and hadronic (e-h) categories. For each event the plots show the best candidate or the combination of candidates for kaons and lambdas, respectively. The sub-taggers were trained and applied to one million B meson pairs after a correct signal-side reconstruction of $B_{sig} \rightarrow J/\Psi K_S^0$. The output for B^0 (\bar{B}^0) is shown in blue (red).

r . The selected track is re-evaluated by another multivariate classifier to improve the separation. As mentioned before, it is important to get the total charge of all candidates for the lambda and kaon category. Therefore, the candidates are combined using Eq. 6.1. The resulting output allows a more precise statement, e.g., the output is reduced if two contradicting candidates are found in one event. Fig. 6.2 shows the resulting qr output for the individual categories after the best-candidate and weighted product selection, respectively. The blue (red) shaded events show candidates originating from a B^0 (\bar{B}^0) meson. The peaks at 0 correspond to an uncertain sub-tagger output, whereas events near to +1 (-1) represent a more reliable tagger information. For most categories, a large peak around 0 indicates wrongly categorized candidates with no flavor information, e.g., pions in the direct electrons category, which is also in good agreement with the low production rates of direct electrons. The intermediate muons allow nearly no extraction of flavor information since they cannot be easily identified in the detector and separated from pions for low momentum. The kaon and slow pion categories show a good separation with small peaks in the middle, since their occurrence is quite high. Moreover, reliable lambda candidates are very rare. It can also be seen, that in the outer regions, the number of wrong tagged events decreases.

In general an asymmetry can be observed in most of the plots, e.g., for direct electrons (indicating a \bar{B}^0) and positrons (indicating a B^0). This effect corresponds to the slightly different production rates of particles and anti-particles in the interaction with the detector material and different detector performances [7].

The final combination is done by another multivariate classifier with the individual categories as input. The classifier output is mapped onto the same range as for the individual categories. A qr value of +1 (-1) indicates a B^0 (\bar{B}^0), while values at 0 represent a random decision. The final result on Monte Carlo can be seen in Fig. 6.3. The combination gives a much better classification of the events; fewer events were evaluated with a random decision. One can also see a decreasing number of wrong tagged events with higher values of the event dilution factor r . The final output is also asymmetrically distributed.

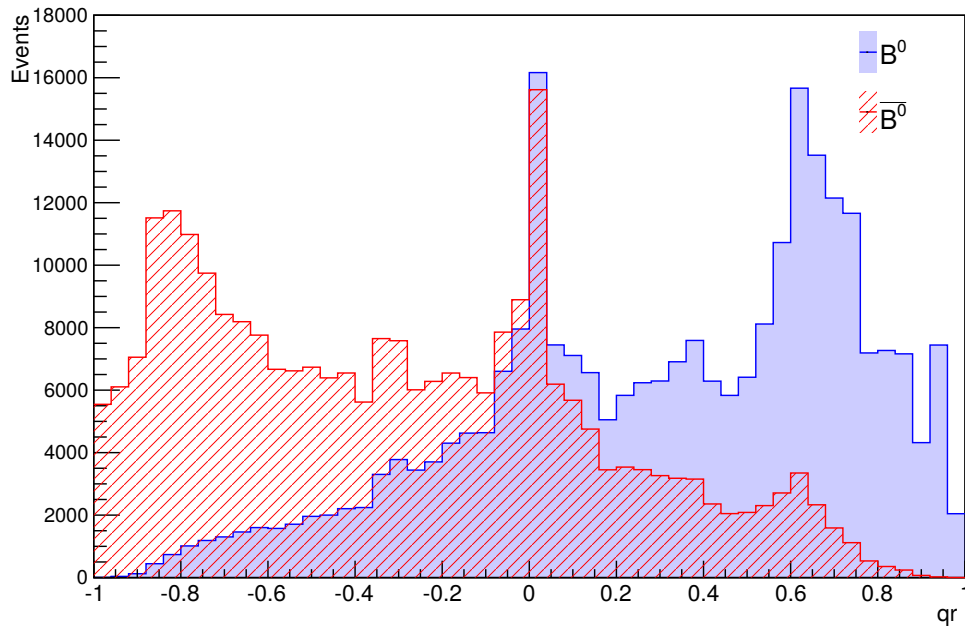


Figure 6.3.: Final output of the Flavor Tagger on signal Monte Carlo. The tagger was trained and applied to one million B meson pairs after a correct signal-side reconstruction of $B_{sig} \rightarrow J/\Psi K_S^0$. The output for B^0 (\bar{B}^0) is shown in blue (red).

6.3

Performance Measurement

The measurement of performance for a Flavor Tagging algorithm is crucial for evaluation and optimization. It has been described for various experiments [33, Chap.8][7]. Here the general approach is presented.

A tagging algorithm cannot always be applied to all events. Thus, the efficiency is defined as

$$\epsilon = \frac{B_t}{B_a}, \quad (6.2)$$

where B_t (B_a) denotes the number of tagged (all) events. It can also come to an incorrect decision, which is represented by the wrong tag fraction

$$\omega = \frac{B_w}{B_c + B_w}, \quad (6.3)$$

where B_w (B_c) denotes the number of wrong (correct) tagged events.

Due to the imperfect efficiency and wrong tagging, the number of tagged events B and \bar{B} are given by

$$\begin{aligned} B &= \epsilon(1 - 2\omega)B^0 + \epsilon\omega\bar{B}^0, \\ \bar{B} &= \epsilon(1 - 2\omega)\bar{B}^0 + \epsilon\omega B^0, \end{aligned} \quad (6.4)$$

where B^0 and \bar{B}^0 represent the physical mesons. The measured asymmetry can be written as

$$A_{meas} = \frac{B - \bar{B}}{B + \bar{B}} = (1 - 2\omega) \frac{B^0 - \bar{B}^0}{B^0 + \bar{B}^0}. \quad (6.5)$$

The physical asymmetry A_{phy} is diluted by a so-called dilution factor D

$$A_{meas} = (1 - 2\omega)A_{phy} = DA_{phy}, \quad (6.6)$$

with a statistical uncertainty of

$$\sigma_{A_{phy}} \propto \frac{1}{\sqrt{\epsilon(1 - 2\omega)}}. \quad (6.7)$$

Therefore, the effective tagging efficiency is defined as

$$\mathcal{Q} = \epsilon(1 - 2\omega)^2. \quad (6.8)$$

The objective is to increase the effective efficiency and thereby decrease the statistical uncertainty for asymmetry measurements. The easiest way to determine the wrong tag fraction would simply be to average over all events, whereas the

most effective way to increase \mathcal{Q} would be to consider each event separately. For a correct simulation of the events and the detector response, the dilution factor for Monte Carlo satisfies

$$r = 1 - 2\omega. \quad (6.9)$$

The direct use of the wrong tag fraction determined on Monte Carlo in an analysis would introduce a systematic bias. Hence, it is measured by fitting $B^0 - \bar{B}^0$ mixing in self-tagging semileptonic and hadronic decay channels, such as $B^0 \rightarrow D^{*-}l^+\nu_l$, $B^0 \rightarrow D^{*-}\pi^+$, $B^0 \rightarrow D^-\pi^+$ and $B^0 \rightarrow D^{*-}\rho^+$ [7].

As a compromise between a high effective efficiency and a feasible measurement of the wrong tag fraction, the events are grouped into bins, according to the event dilution factor. Under the assumption of a correct Monte Carlo, the average dilution factor of each bin and the wrong tag fraction still approximately fulfills Eq. 6.9. In Belle and BaBar the efficiency was calculated by dividing the events into 6 and 7 bins, respectively. The effective efficiency is then calculated as

$$\mathcal{Q} = \sum_{i=1}^6 \epsilon_i (1 - 2\omega_i)^2, \quad (6.10)$$

where ϵ_i (ω_i) denotes the event (wrong tag) fraction in the corresponding bin i . Since this work is based on Belle, the same bin separation is used: $0 \leq r \leq 0.25$, $0.25 < r \leq 0.5$, $0.5 < r \leq 0.625$, $0.625 < r \leq 0.75$, $0.75 < r \leq 0.875$ and $0.875 < r \leq 1$ [7]. Tab. 6.1 shows the average of 10 runs for the actual approach compared to Belle results on Monte Carlo. The individual efficiencies are calculated with the same method. The wrong tag fraction was extracted directly from the Monte Carlo. Each run was trained and evaluated on one million $B^0\bar{B}^0$ pairs, in order to cope with fluctuations due to the trained methods and the Monte Carlo production. No overtraining was observed for the used classifiers.

Although the setups between Belle and Belle II differ in event and detector simulation as well as in other aspects like tracking, the numbers in Tab. 6.1 give a qualitative overview. It has to be noted that the individual efficiencies cannot be added up since the categories are to some extent overlapping. High momentum pions were not considered separately at Belle, but were found in the kaon and muon category. As expected, kaons have the most powerful separation power. Slow pions give also much flavor information as well as leptons with high momentum since they can be clearly identified. The total effective efficiency on Monte Carlo data increased by $\sim 3.1\%$ compared to Belle.

Table 6.1.: Comparison of individual and total effective efficiencies between Belle II and Belle on Monte Carlo data [7]. The Flavor Tagger for Belle II was trained and applied to one million B meson pairs after the signal-side reconstruction of $B_{sig} \rightarrow J/\Psi K_S^0$. The results are averaged over 10 independent datasets.

| Belle II | $\mathcal{Q}_{cat}(\%)$ | Belle | $\mathcal{Q}_{cat}(\%)$ |
|-------------------------------|--|---------------|-------------------------|
| e_{direct}^+ | 5.06 ± 0.07 | Leptons | 12 |
| $e_{secondary}^+$ | 0.70 ± 0.11 | | |
| μ_{direct}^+ | 5.60 ± 0.06 | | |
| $\mu_{secondary}^+$ | 0.02 ± 0.00 | | |
| K^+ | 12.12 ± 0.08 | Slow Pion | 6 |
| π_{slow}^+ | 6.62 ± 0.06 | | |
| $\pi_{high\ mom}^+$ | 1.67 ± 0.13 | | |
| Λ^0 | 1.66 ± 0.12 | Kaon + Lambda | 18 |
| Eff. efficiency \mathcal{Q} | $(32.44 \pm 0.09)\%$ | | |
| | | | 29.3 % |

6.4

Integration of the Full Event Interpretation

As already mentioned, Flavor Tagging follows an inclusive approach where only final state particles (and reconstructed lambdas) are taken into account. Information about D mesons is only indirectly available via final state particles since they are not explicitly reconstructed. Nonetheless, this information is valuable for the flavor determination of a tag-side B meson.

In contrast, another analysis tool of basf2, the Full Event Interpretation, does a complete and explicit reconstruction of hadronic and semileptonic decay channels [8]. It follows a hierarchical approach starting with final state particles which are combined in different decay channels up to the mother B meson. For the evaluation of the reconstructed particles multivariate classifiers are used. At

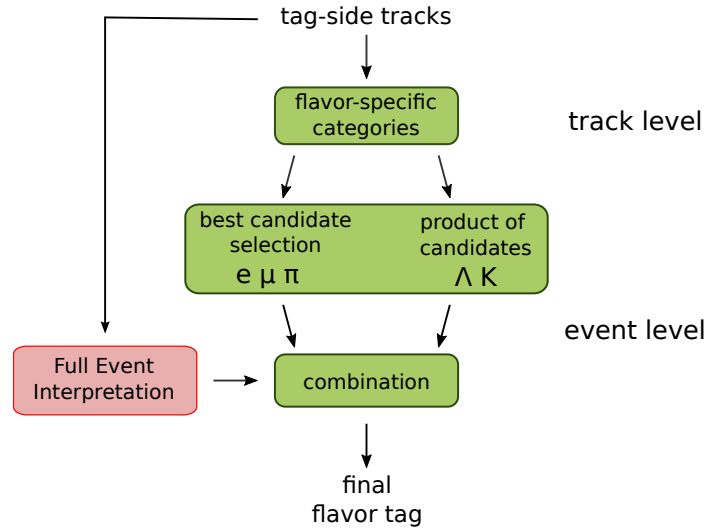


Figure 6.4.: Flavor Tagging with the additional Full Event Interpretation.

the time of writing the following reconstructed D mesons from various decay channels are included into Flavor Tagging: D^{*+} , D_s^{*+} , D_s^+ , D^{*0} , D^+ , D^{*0} and D^0 . In addition, fully reconstructed B mesons from hadronic B_{had}^0 , semileptonic $B_{semilep}^0$ and semileptonic decays involving a D meson $B_{semilepD}^0$ are considered. The multivariate methods are trained independently on 10 million mono-generic¹ Monte Carlo events. The target is to separate correctly reconstructed particles, while intermediate resonances and neutrinos from semileptonic channels are neglected. A complete list of the reconstructed decay channels can be found in Appendix B. For more details on the Implementation of the Full Event Interpretation the reader is referred to [8].

The Full Event Interpretation runs completely independent on the tag-side; the

¹The signal-side decays to two neutrinos, see Sec. 5.3.

Table 6.2.: Results for individual and total effective efficiencies for the Flavor Tagging with included categories of the Full Event Interpretation. The Flavor Tagger was trained and applied to one million B meson pairs after the signal-side reconstruction of $B_{sig} \rightarrow J/\Psi K_S^0$. The results are averaged over 10 independent datasets.

| | $\mathcal{Q}_{cat}(\%)$ | | $\mathcal{Q}_{cat}(\%)$ |
|-------------------------------|--|------------------|-------------------------|
| e_{direct}^+ | 5.02 ± 0.05 | D^{*+} | 3.30 ± 0.03 |
| $e_{secondary}^+$ | 0.67 ± 0.10 | D_s^{*+} | 0.18 ± 0.01 |
| μ_{direct}^+ | 5.60 ± 0.09 | D_s^+ | 0.47 ± 0.02 |
| $\mu_{secondary}^+$ | 0.02 ± 0.00 | D^+ | 2.27 ± 0.05 |
| K^+ | 12.12 ± 0.08 | D^{*0} | 0.39 ± 0.02 |
| π_{slow}^+ | 6.66 ± 0.04 | D^0 | 2.51 ± 0.04 |
| $\pi_{high\ mom}^+$ | 1.63 ± 0.14 | B_{had}^0 | 0.90 ± 0.01 |
| Λ^0 | 1.63 ± 0.13 | $B_{semilep}^0$ | 3.00 ± 0.02 |
| | | $B_{semilepD}^0$ | 3.41 ± 0.06 |
| <hr/> | | | |
| Eff. efficiency \mathcal{Q} | $(32.79 \pm 0.08)\%$ | | |

information of the additional categories is then included into the final combination. The sub-tagger output from the Full Event Interpretation after a best candidate selection can be seen in Fig. 6.5. In order to measure the effect on the final tagging output, the categories are evaluated with the same method as described above. Tab. 6.2 shows the individual efficiencies for all categories.

Although the additional D and B meson categories give small flavor information, their impact on the total effective efficiency is only of the order of $O(0.1)\%$. For the exclusive reconstruction of such a meson sufficient final state particles are required. These final state particles are of course also available for the inclusive methods and hence no or very less additional information is gained, e.g., the reconstruction of a D^{*+} requires a good slow pion candidate which was already evaluated by the slow pion category. Without any inclusive categories the impact of the Full Event Interpretation for Flavor Tagging was found to be $\sim 11.4\%$. This illustrates that in principle an inclusive approach as a tagging algorithm is preferable.

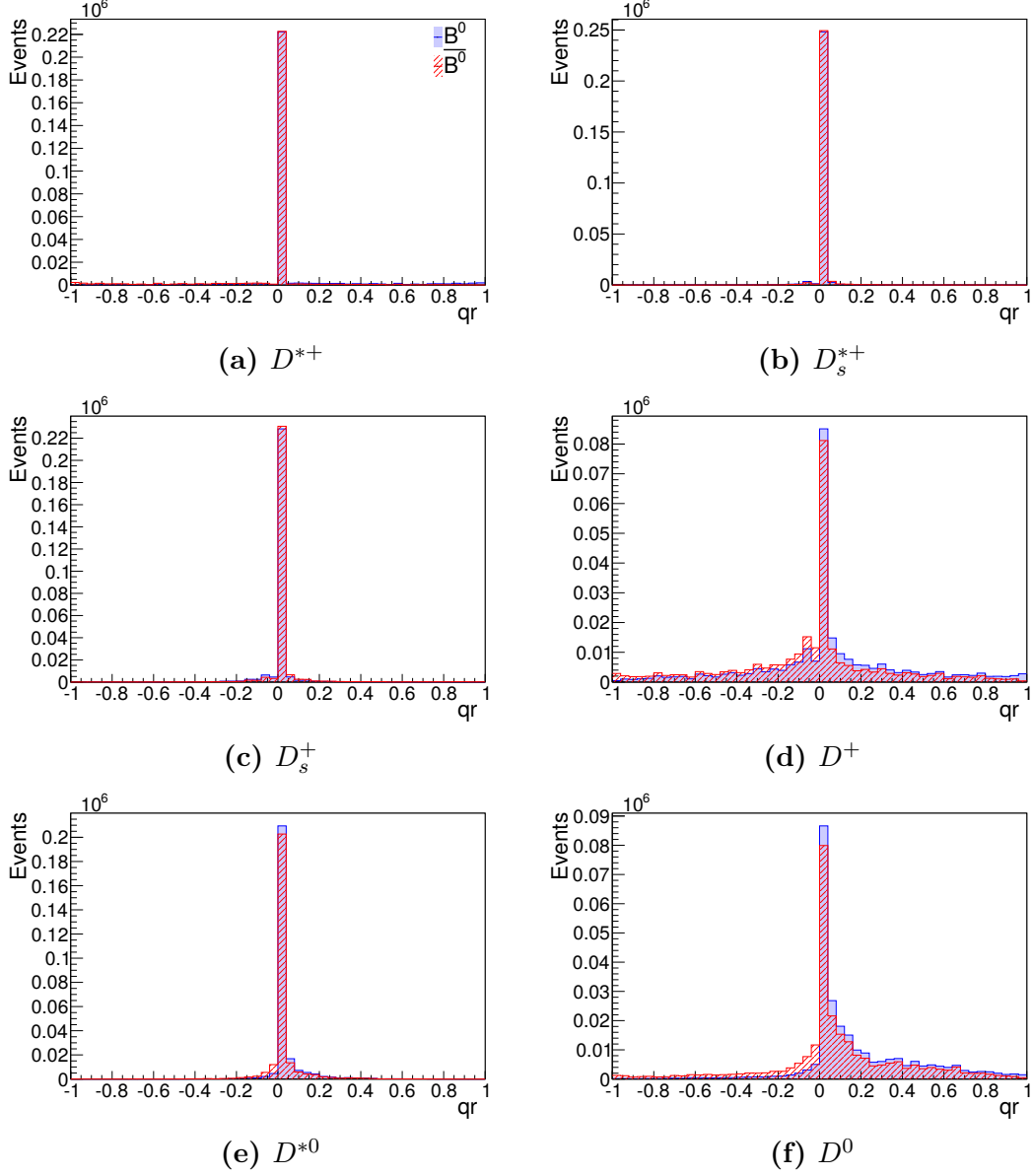


Figure 6.5.: Output of the D meson sub-taggers of the Full Event Interpretation. The plots show the best candidate for each event. The external classifiers were trained on a mono-generic Monte Carlo sample and were applied to one million B meson pairs after a correct signal-side reconstruction of $B_{sig} \rightarrow J/\Psi K_S^0$. The output for B^0 (\bar{B}^0) is shown in blue (red).

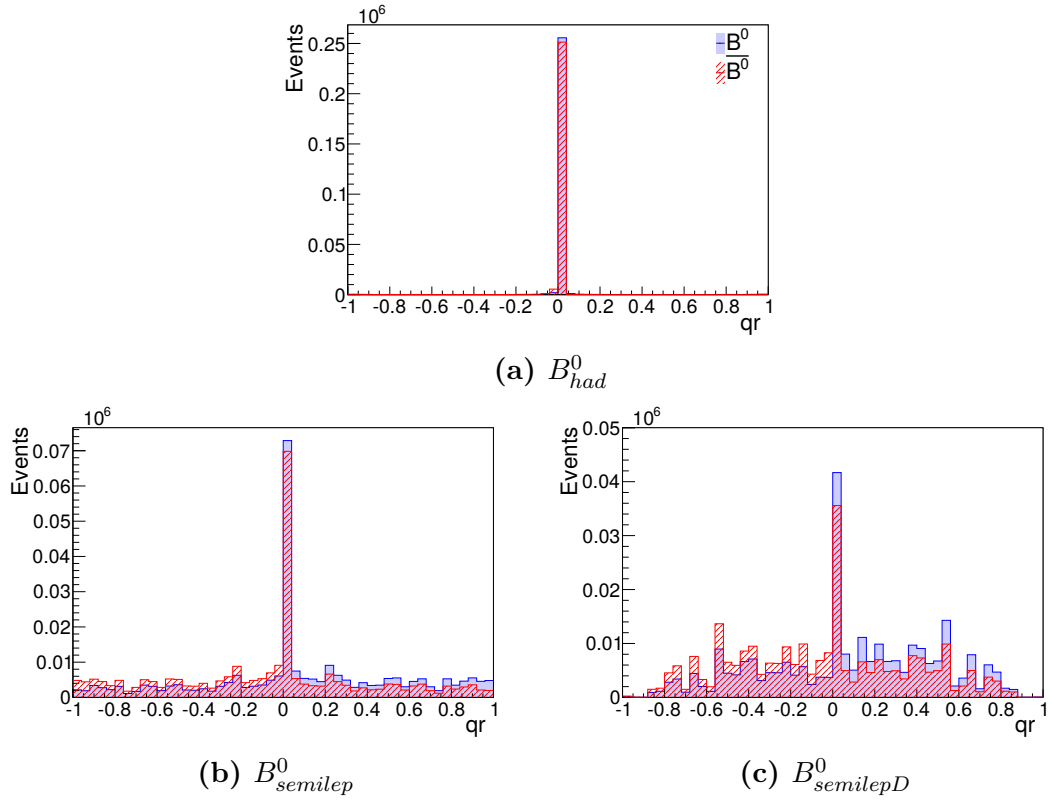


Figure 6.6.: Output of the B meson sub-taggers of the Full Event Interpretation. The plots show the best candidate for each event. The external classifiers were trained on a mono-generic Monte Carlo sample and were applied to one million B meson pairs after a correct signal-side reconstruction of $B_{sig} \rightarrow J/\Psi K_S^0$. The output for B^0 (\bar{B}^0) is shown in blue (red).

CHAPTER 7

Conclusion

In this work, the implementation of Flavor Tagging for the Belle II Experiment is presented. It is integrated into the Belle II Analysis Framework and will be used for the measurement of mixing-induced CP violation in various decay channels. The structure follows the approach of the Belle Experiment. After the reconstruction of the desired signal-side to a CP eigenstate, Flavor Tagging is applied on the remaining track candidates of the tag-side. The process is divided into a track and an event level. At track level different flavor-specific categories are introduced, such as leptons, pions, kaons and lambdas. The track candidates are evaluated according to their input variables. The information of the individual sub-taggers are combined on event level by a multivariate classifier, which gives a final flavor tag for the B meson.

The performance of the algorithm is measured by the effective efficiency. At the time of writing no data was available, therefore it was determined on Monte Carlo as

$$Q = 32.44\%.$$

This is an improvement of $\sim 3.1\%$ compared to Belle [7].

Flavor Tagging is further improved by the integration of the Full Event Interpretation, which reconstructs a large number of modes exclusively. Hence, flavor information from reconstructed D and B mesons can also be taken into account. At the time of writing it was found to give an increase in effective efficiency of the order of $O(0.1)\%$. As the Flavor Tagging as well as the Full Event Interpretation will be further optimized in the future, the effective efficiency will increase.

APPENDIX A

Training Variables

Table A.1.: List of track level variables for direct and secondary electron candidates.

| Variable | Description |
|--------------------|--|
| p_{cms} | Center-of-mass momentum |
| pt_{cms} | Center-of-mass transverse momentum |
| eid | Electron identification probability |
| eid_dEdx | Electron identification probability from dE/dx measurement |
| eid_TOP | Electron identification probability from TOP |
| eid_ARICH | Electron identification probability from ARICH |
| eid_ECL | Electron identification probability from ECL |
| $cos\Theta_{lab}$ | Cosine of the polar angle in the laboratory frame |
| q | Charge of the track |
| M_{recoil} | Hadronic recoil mass |
| p_{miss} | Missing momentum on the tag-side |
| $cos\Theta_{miss}$ | Cosine of the angle between the lepton and the missing momentum |
| $EW90$ | Center-of-mass energy in the hemisphere of the virtual W boson and the B_{tag} meson |

Table A.2.: List of track level variables for direct and secondary muon candidates.

| Variable | Description |
|---------------------|--|
| p_{cms} | Center-of-mass momentum |
| pt_{cms} | Center-of-mass transverse momentum |
| $muid$ | Muon identification probability |
| $muid_{dEdx}$ | Muon identification probability from dE/dx measurement |
| $muid_{TOP}$ | Muon identification probability from TOP |
| $muid_{ARICH}$ | Muon identification probability from ARICH |
| $\cos\Theta_{lab}$ | Cosine of the polar angle in the laboratory frame |
| q | Charge of the track |
| M_{recoil} | Hadronic recoil mass |
| p_{miss} | Missing momentum on the tag-side |
| $\cos\Theta_{miss}$ | Cosine of the angle between the lepton and the missing momentum |
| $EW90$ | Center-of-mass energy in the hemisphere of the virtual W boson and the B_{tag} meson |

Table A.3.: List of track level variables for kaon candidates.

| Variable | Description |
|--------------------|---|
| p_{cms} | Center-of-mass momentum |
| pt_{cms} | Center-of-mass transverse momentum |
| Kid | Kaon identification probability |
| Kid_{dEdx} | Kaon identification probability from dE/dx measurement |
| Kid_{TOP} | Kaon identification probability from TOP |
| Kid_{ARICH} | Kaon identification probability from ARICH |
| $\cos\Theta_{lab}$ | Cosine of the polar angle in the laboratory frame |
| q | Charge of the track |
| $N(K_S^0)$ | Number of K_S^0 on the tag-side |
| $ptTracksRoe$ | Transverse momentum of all charged tracks on the tag-side |
| d | Distance relative to the interaction point |
| $chiProb$ | χ^2 probability of the fit |

Table A.4.: List of track level variables for slow and high momentum pion candidates.

| Variable | Description |
|----------------------|---|
| p_{cms} | Center-of-mass momentum |
| pt_{cms} | Center-of-mass transverse momentum |
| $piid$ | Pion identification probability |
| $piid_{dEdx}$ | Pion identification probability from dE/dx measurement |
| pi_vs_edEdx | Pion vs electron identification probability |
| $piid_{TOP}$ | Pion identification probability from TOP |
| $piid_{ARICH}$ | Pion identification probability from ARICH |
| Kid | Kaon identification probability |
| eid | Electron identification probability |
| $cos\Theta_{lab}$ | Cosine of the polar angle in the laboratory frame |
| $cos\alpha_{thrust}$ | Cosine of angle between thrust axis of given particle and thrust axis of the tag-side |
| q | Charge of the track |
| $N(K_S^0)$ | Number of K_S^0 on the tag-side |
| $ptTracksRoe$ | Transverse momentum of all charged tracks on tag-side |
| d | Distance relative to the interaction point |
| $chiProb$ | χ^2 probability of the fit |

Table A.5.: List of track level variables for lambda candidates.

| Variable | Description |
|---------------------|---|
| p_{cms} | Center-of-mass momentum |
| M | Invariant mass |
| $\cos\alpha_p$ | Cosine of angle between momentum and vertex vector (vector connecting IP and fitted vertex) |
| $lambdaZError$ | z difference of the pion and proton track at the lambda vertex |
| $p_{sec. daughter}$ | Momentum of second daughter |
| $lambdaFlavor$ | Flavor of the lambda |
| $N(K_S^0)$ | Number of K_S^0 on the tag-side |
| d | Distance relative to the interaction point |
| $chiProb$ | χ^2 probability of the fit |

Table A.6.: List of event level variables.

| Variable | Description |
|-------------------------|---|
| $(qr)_{direct\ e}$ | qr value of the best candidate from the primary electron category |
| $(qr)_{secondary\ e}$ | qr value of the best candidate from the secondary electron category |
| $(qr)_{direct\ \mu}$ | qr value of the best candidate from the primary muon category |
| $(qr)_{secondary\ \mu}$ | qr value of the best candidate from the secondary muon category |
| $(qr)_{slow\ \pi}$ | qr value of the best candidate from the slow pion category |
| $(qr)_{high\ mom\ \mu}$ | qr value of the best candidate from the high momentum pion category |
| $(qr)_K$ | qr value of the weighted product from the kaon category |
| $(qr)_\Lambda$ | qr value of the weighted product from the lambda category |

Table A.7.: List of event level variables integrated with the Full Event Interpretation.

| Variable | Description |
|-------------------------|---|
| $(qr)_{direct\ e}$ | qr value of the best candidate from the primary electron category |
| $(qr)_{secondary\ e}$ | qr value of the best candidate from the secondary electron category |
| $(qr)_{direct\ \mu}$ | qr value of the best candidate from the primary muon category |
| $(qr)_{secondary\ \mu}$ | qr value of the best candidate from the secondary muon category |
| $(qr)_{slow\ \pi}$ | qr value of the best candidate from the slow pion category |
| $(qr)_{high\ mom\ \mu}$ | qr value of the best candidate from the high momentum pion category |
| $(qr)_K$ | qr value of the weighted product from the kaon category |
| $(qr)_\Lambda$ | qr value of the weighted product from the lambda category |
| $(qr)_{D^{*+}}$ | qr value of the best candidate from D^{*+} category |
| $(qr)_{D_s^{*+}}$ | qr value of the best candidate from D_s^{*+} category |
| $(qr)_{D_s^+}$ | qr value of the best candidate from D_s^+ category |
| $(qr)_{D^+}$ | qr value of the best candidate from D^+ category |
| $(qr)_{D^{*0}}$ | qr value of the best candidate from D^{*0} category |
| $(qr)_{D^0}$ | qr value of the best candidate from D^0 category |
| $(qr)_{B_{had}^0}$ | qr value of the best candidate from B_{had}^0 category |
| $(qr)_{B_{semilep}^0}$ | qr value of the best candidate from $B_{semilep}^0$ category |
| $(qr)_{B_{semilepD}^0}$ | qr value of the best candidate from $B_{semilepD}^0$ category |

APPENDIX B

Decay Channels of the Full Event Interpretation

The decay channels which were used for the categories of the Full Event Interpretation are listed in the following. For more information the reader is referred to [8].

 D^{*+}

- $D^{*+} \rightarrow D^0 \pi^+$
- $D^{*+} \rightarrow D^+ \pi^0$

 D_s^{*+}

- $D_s^{*+} \rightarrow D_s^+ \gamma$
- $D_s^{*+} \rightarrow D_s^+ \pi^0$

 D_s^+

- $D_s^+ \rightarrow K^+ K_S^0$
- $D_s^+ \rightarrow K^+ \pi^+ \pi^-$
- $D_s^+ \rightarrow K^+ K^- \pi^+$
- $D_s^+ \rightarrow K^+ K^- \pi^+ \pi^0$
- $D_s^+ \rightarrow K^+ K_S^0 \pi^+ \pi^-$

- $D_s^+ \rightarrow K^- K_S^0 \pi^+ \pi^+$
- $D_s^+ \rightarrow K^+ K^- \pi^+ \pi^+ \pi^-$
- $D_s^+ \rightarrow \pi^+ \pi^+ \pi^-$
- $D_s^+ \rightarrow K_S^0 \pi^+ \pi^0$

 D^+

- $D^+ \rightarrow K^- \pi^+ \pi^+$
- $D^+ \rightarrow K^- \pi^+ \pi^+ \pi^0$
- $D^+ \rightarrow K^- K^+ \pi^+$
- $D^+ \rightarrow K^- K^+ \pi^+ \pi^0$
- $D^+ \rightarrow \pi^+ \pi^0$
- $D^+ \rightarrow \pi^+ \pi^+ \pi^-$
- $D^+ \rightarrow \pi^+ \pi^+ \pi^- \pi^0$
- $D^+ \rightarrow K_S^0 \pi^+$
- $D^+ \rightarrow K_S^0 \pi^+ \pi^0$
- $D^+ \rightarrow K_S^0 \pi^+ \pi^+ \pi^-$
- $D^+ \rightarrow K^+ K_S^0 K_S^0$

 D^{*0}

- $D^{0*} \rightarrow D^0 \pi^0$
- $D^{0*} \rightarrow D^0 \gamma$

 D^0

- $D^0 \rightarrow K^- \pi^+$
- $D^0 \rightarrow K^- \pi^+ \pi^0$
- $D^0 \rightarrow K^- \pi^+ \pi^0 \pi^0$
- $D^0 \rightarrow K^- \pi^+ \pi^+ \pi^-$

-
- $D^0 \rightarrow K^- \pi^+ \pi^+ \pi^- \pi^0$
 - $D^0 \rightarrow \pi^- \pi^+$
 - $D^0 \rightarrow \pi^- \pi^+ \pi^+ \pi^-$
 - $D^0 \rightarrow \pi^- \pi^+ \pi^0$
 - $D^0 \rightarrow \pi^- \pi^+ \pi^0 \pi^0$
 - $D^0 \rightarrow K_S^0 \pi^0$
 - $D^0 \rightarrow K_S^0 \pi^+ \pi^-$
 - $D^0 \rightarrow K_S^0 \pi^+ \pi^- \pi^0$
 - $D^0 \rightarrow K^- K^+$
 - $D^0 \rightarrow K^- K^+ \pi^0$
 - $D^0 \rightarrow K^- K^+ K_S^0$

 B_{had}^0

- $B^0 \rightarrow D^- \pi^+$
- $B^0 \rightarrow D^- \pi^0 \pi^+$
- $B^0 \rightarrow D^- \pi^+ \pi^+ \pi^-$
- $B^0 \rightarrow \bar{D}^0 \pi^+ \pi^-$
- $B^0 \rightarrow D^{*-} \pi^+$
- $B^0 \rightarrow D^{*-} \pi^0 \pi^+$
- $B^0 \rightarrow D^{*-} \pi^+ \pi^+ \pi^-$
- $B^0 \rightarrow D^{*-} \pi^+ \pi^+ \pi^- \pi^0$

 $B_{semilep}^0$

- $B^0 \rightarrow D^- e^+$
- $B^0 \rightarrow D^- \mu^+$
- $B^0 \rightarrow D^{*-} e^+$
- $B^0 \rightarrow D^{*-} \mu^+$
- $B^0 \rightarrow \bar{D}^0 \pi^- e^+$
- $B^0 \rightarrow \bar{D}^0 \pi^- \mu^+$
- $B^0 \rightarrow \text{anti-}D^{0*} \pi^- e^+$
- $B^0 \rightarrow \text{anti-}D^{0*} \pi^- \mu^+$

 $B_{semilepD}^0$

- $B^0 \rightarrow D^- \pi^+$
- $B^0 \rightarrow D^- \pi^0 \pi^+$
- $B^0 \rightarrow D^- \pi^+ \pi^+ \pi^-$
- $B^0 \rightarrow D^- e^+$
- $B^0 \rightarrow D^- \mu^+$
- $B^0 \rightarrow \bar{D}^0 \pi^- e^+$
- $B^0 \rightarrow \bar{D}^0 \pi^- \mu^+$

Bibliography

- [1] K. Abe et al. Observation of large cp violation and evidence for direct cp violation in $B^0 \rightarrow \pi^+\pi^-$ decays. *Phys. Rev. Lett.*, 93:021601, Jul 2004. doi: 10.1103/PhysRevLett.93.021601. URL <http://link.aps.org/doi/10.1103/PhysRevLett.93.021601>.
- [2] K. Abe et al. Measurement of time dependent CP violating asymmetries in $B^0 \rightarrow \phi K^0(s)$, $K^+ K^- K^0(s)$, and η' - $K^0(s)$ decays. *Phys.Rev.Lett.*, 91:261602, 2003. doi: 10.1103/PhysRevLett.91.261602.
- [3] The nobel prize in physics 2008. *Nobel Media AB 2014*, 18.04.2015. URL http://www.nobelprize.org/nobel_prizes/physics/laureates/2008/.
- [4] K. Ikado et al. Evidence of the purely leptonic decay $B^- \rightarrow \tau^- \bar{\nu}_\tau$. *Phys. Rev. Lett.*, 97:251802, Dec 2006. doi: 10.1103/PhysRevLett.97.251802. URL <http://link.aps.org/doi/10.1103/PhysRevLett.97.251802>.
- [5] B.R. Ko et al. Observation of $D^0 - \bar{D}^0$ Mixing in e^+e^- Collisions. *Phys.Rev.Lett.*, 112:111801, 2014. doi: 10.1103/PhysRevLett.112.111801.
- [6] S.-K. Choi et al. Observation of a narrow charmoniumlike state in exclusive $b^\pm \rightarrow k^\pm \pi^+ \pi^- j/\psi$ decays. *Phys. Rev. Lett.*, 91:262001, Dec 2003. doi: 10.1103/PhysRevLett.91.262001.
- [7] H. Kakuno et al. Neutral B flavor tagging for the measurement of mixing induced CP violation at Belle. *Nucl.Instrum.Meth.*, A533:516–531, 2004. doi: 10.1016/j.nima.2004.06.159.
- [8] Th. Keck. The Full Event Interpretation for Belle II. *not published*, 2014. URL <http://ekp-invenio.physik.uni-karlsruhe.de/record/48602>.

- [9] Z. Doležal and S. Uno. Belle II Technical Design Report. *not published*, 2010.
- [10] *online*, 18.03.2015. URL http://belle2.desy.de/sites2009/site_belle2/content/e103206/e103207/SuperKEKB:BelleII.jpg.
- [11] J. Kemmer and G. Lutz. New detector concepts. *Nuclear Instruments and Methods in Physics Research Section A: Accelerators, Spectrometers, Detectors and Associated Equipment*, 253(3):365 – 377, 1987. ISSN 0168-9002. doi: [http://dx.doi.org/10.1016/0168-9002\(87\)90518-3](http://dx.doi.org/10.1016/0168-9002(87)90518-3). URL <http://www.sciencedirect.com/science/article/pii/0168900287905183>.
- [12] V. Aulchenko et al. Electromagnetic calorimeter for belle ii. *Journal of Physics: Conference Series*, 587(1):012045, 2015. URL <http://stacks.iop.org/1742-6596/587/i=1/a=012045>.
- [13] *online*, 22.03.2015. URL http://en.wikipedia.org/wiki/File:Standard_Model_of_Elementary_Particles.svg.
- [14] N. Cabibbo. Unitary symmetry and leptonic decays. *Phys. Rev. Lett.*, 10: 531–533, Jun 1963. doi: 10.1103/PhysRevLett.10.531. URL <http://link.aps.org/doi/10.1103/PhysRevLett.10.531>.
- [15] M. Kobayashi and T. Maskawa. Cp-violation in the renormalizable theory of weak interaction. *Progress of Theoretical Physics*, 49(2):652–657, 1973. doi: 10.1143/PTP.49.652. URL <http://ptp.oxfordjournals.org/content/49/2/652.abstract>.
- [16] L. Wolfenstein. Parametrization of the kobayashi-maskawa matrix. *Phys. Rev. Lett.*, 51:1945–1947, Nov 1983. doi: 10.1103/PhysRevLett.51.1945. URL <http://link.aps.org/doi/10.1103/PhysRevLett.51.1945>.
- [17] J. Charles et al. Cp violation and the ckm matrix: assessing the impact of the asymmetric b factories. *Eur. Phys. J.*, C41(1):1–131, 2005. ISSN 1434-6044. doi: 10.1140/epjc/s2005-02169-1. Updated results and plots available at <http://ckmfitter.in2p3.fr>.
- [18] Th. Kuhr. *Flavor Physics at the Tevatron*. Springer-Verlag Berlin Heidelberg, 2013. doi: 10.1007/978-3-642-10300-1.
- [19] B. Aubert et al. Direct *cp* violating asymmetry in $B^0 \rightarrow K^+ \pi^-$ decays. *Phys. Rev. Lett.*, 93:131801, Sep 2004. doi: 10.1103/PhysRevLett.93.131801. URL <http://link.aps.org/doi/10.1103/PhysRevLett.93.131801>.
- [20] I. Adachi and others. Precise measurement of the *cp* violation parameter $\sin 2\phi_1$ in $B^0 \rightarrow (c\bar{c})K^0$ decays. *Phys. Rev. Lett.*, 108:171802, Apr 2012.

- doi: 10.1103/PhysRevLett.108.171802. URL <http://link.aps.org/doi/10.1103/PhysRevLett.108.171802>.
- [21] B. Aubert et al. Measurement of time-dependent cp asymmetry in $B^0 \rightarrow c\bar{c}K^{(*)0}$ decays. *Phys. Rev. D*, 79:072009, Apr 2009. doi: 10.1103/PhysRevD.79.072009. URL <http://link.aps.org/doi/10.1103/PhysRevD.79.072009>.
- [22] S. Neubauer. Search for $b \rightarrow k^{(*)}\nu\bar{\nu}$ decays using a new probabilistic full reconstruction method. *not published*, 2011. URL <https://ekp-invenio.physik.uni-karlsruhe.de/record/48215>.
- [23] A. Hocker, J. Stelzer, F. Tegenfeldt, H. Voss, K. Voss, et al. TMVA - Toolkit for Multivariate Data Analysis. *PoS, ACAT:040*, 2007.
- [24] R. A. Fisher. The use of multiple measurements in taxonomic problems. *Annals of Eugenics*, 7(2):179–188, 1936. doi: 10.1111/j.1469-1809.1936.tb02137.x.
- [25] M. Feindt and U. Kerzel. The neurobayes neural network package. *Nuclear Instruments and Methods in Physics Research Section A: Accelerators, Spectrometers, Detectors and Associated Equipment*, 559(1):190 – 194, 2006. doi: <http://dx.doi.org/10.1016/j.nima.2005.11.166>.
- [26] J.H. Friedman. Stochastic gradient boosting. *Computational Statistics & Data Analysis*, 38(4):367 – 378, 2002. doi: [http://dx.doi.org/10.1016/S0167-9473\(01\)00065-2](http://dx.doi.org/10.1016/S0167-9473(01)00065-2).
- [27] V. Blobel and E. Lohrmann. *Statistische und numerische Methoden der Datenanalyse*. Teubner-Studienbücher : Physik. 1998. URL <http://books.google.de/books?id=NcIxajwHOZIC>.
- [28] Y. Freund and R.E. Schapire. A decision-theoretic generalization of on-line learning and an application to boosting. *Journal of Computer and System Sciences*, 55(1):119 – 139, 1997. ISSN 0022-0000. doi: <http://dx.doi.org/10.1006/jcss.1997.1504>. URL <http://www.sciencedirect.com/science/article/pii/S002200009791504X>.
- [29] J. H. Friedman. Greedy function approximation: A gradient boosting machine. *Ann. Statist.*, 29(5):1189–1232, 10 2001. doi: 10.1214/aos/1013203451. URL <http://dx.doi.org/10.1214/aos/1013203451>.
- [30] Anders Ryd, David Lange, Natalia Kuznetsova, Sophie Versille, Marcello Rotondo, et al. EvtGen: A Monte Carlo Generator for B-Physics. 2005.
- [31] S. Agostinelli et al. GEANT4: A Simulation toolkit. *Nucl.Instrum.Meth.*, A506:250–303, 2003. doi: 10.1016/S0168-9002(03)01368-8.

- [32] K.A. Olive et al. Review of Particle Physics. *Chin.Phys.*, C38:090001, 2014.
doi: 10.1088/1674-1137/38/9/090001.
- [33] A.J. Bevan et al. The Physics of the B Factories. *Eur.Phys.J.*, C74(11):3026,
2014. doi: 10.1140/epjc/s10052-014-3026-9.

List of Figures

| | | |
|------|--|-----|
| 0.1. | Rekonstruktion des CP-Eigenzustandes auf der Signal-Seite f_{CP} . Die Spuren der Tag-Seite f_{tag} werden für das Flavor Tagging verwendet. | ii |
| 0.2. | Finale Ausgabe des Flavor Taggings auf simulierten Monte Carlo Daten. Der Tagger wurde auf eine Million B -Mesonpaare nach korrekter Rekonstruktion der Signal-Seite trainiert und angewendet. Die Ausgabe für $B^0(\bar{B}^0)$ -Mesonen ist in blau (rot) dargestellt. . . | iii |
| 2.1. | Scheme of the SuperKEKB accelerator. The lower part shows the Linac which injects electrons and positrons into the HER, LER respectively. The beams collide at the interaction point in the Belle II detector with a center-of-mass energy of $\sqrt{s} = 10.58$ GeV. Taken from [10]. | 4 |
| 2.2. | Model of the PXD which is placed next to the interaction point. Its innermost layer has a radius of 14 mm, the outer layer one of 22 mm, respectively. [9]. | 6 |
| 2.3. | Scheme of the SVD with its four layers of double-sided silicon strip detectors and the beampipe with PXD in the middle. Taken from [9]. | 7 |
| 2.4. | Scheme of the CDC with its nine superlayers containing six layers. The two innermost layers serve as guards for the high background. Taken from [9]. | 7 |
| 2.5. | Picture of a time-of-propagation detector bar. Pions and Kaons emit Cherenkov photons within cones of different angles which gives a distinction. Taken from [9]. | 8 |
| 2.6. | Schematic view of the ARICH. Charged particles emit photons in the aerogel medium which propagate through a volume to a photon detector. Taken from [9]. | 8 |

| | | |
|------|--|----|
| 2.7. | Cut through the Belle II detector. The interaction point in the middle is surrounded by the PXD and SVD for a close vertex measurement, surrounded by the CDC for track reconstruction. It is followed by the PID and ECL. The outermost part for K_L and muon identification is given by the KLM. Taken from [9]. | 10 |
| 3.1. | Overview of the Standard Model with its three generations of fermions, the gauge and Higgs bosons. Taken from [13]. | 12 |
| 3.2. | Actual constraints for the measurement of $\bar{\rho}$ and $\bar{\eta}$ [17]. | 14 |
| 4.1. | Production of B meson pairs at the $\Upsilon(4S)$ resonance. Taken from [22]. | 17 |
| 4.2. | Reconstruction of the CP eigenstate on the signal-side f_{CP} , the tracks on the tag-side f_{tag} are used for Flavor Tagging. | 18 |
| 4.3. | Production process for direct leptons. | 19 |
| 4.4. | Distribution of p_{cms} (left) and $\cos\theta_{miss}$ (right) for direct (solid) and secondary (hashed) muons on Monte Carlo, see Sec. 5.3. | 20 |
| 4.5. | Production process for slow pions. | 20 |
| 4.6. | Distribution of p_{cms} (left) and α_{thrust} (right) for slow (solid) and high momentum (hashed) pions on Monte Carlo, see Sec. 5.3. | 21 |
| 4.7. | Production process for kaons. | 21 |
| 4.8. | Production process for lambdas. | 22 |
| 5.1. | Structure of a decision tree. | 24 |
| 5.2. | Example of a ROC curve plot provided by TMVA. It shows signal efficiency against background rejection. | 26 |
| 5.3. | Example of an overtraining check provided by TMVA. It shows the results for training (dots) and test sample (shaded area) for the signal and background distribution. The Kolmogorov-Smirnov test also allows to check for overtraining. | 26 |
| 6.1. | General approach of the Flavor Tagging. | 30 |
| 6.2. | Output of the sub-taggers for leptonic (a-d) and hadronic (e-h) categories. For each event the plots show the best candidate or the combination of candidates for kaons and lambdas, respectively. The sub-taggers were trained and applied to one million B meson pairs after a correct signal-side reconstruction of $B_{sig} \rightarrow J/\Psi K_S^0$. The output for B^0 (\bar{B}^0) is shown in blue (red). | 31 |
| 6.3. | Final output of the Flavor Tagger on signal Monte Carlo. The tagger was trained and applied to one million B meson pairs after a correct signal-side reconstruction of $B_{sig} \rightarrow J/\Psi K_S^0$. The output for B^0 (\bar{B}^0) is shown in blue (red). | 33 |
| 6.4. | Flavor Tagging with the additional Full Event Interpretation. | 37 |

-
- 6.5. Output of the D meson sub-taggers of the Full Event Interpretation. The plots show the best candidate for each event. The external classifiers were trained on a mono-generic Monte Carlo sample and were applied to one million B meson pairs after a correct signal-side reconstruction of $B_{sig} \rightarrow J/\Psi K_S^0$. The output for B^0 (\bar{B}^0) is shown in blue (red). 39
- 6.6. Output of the B meson sub-taggers of the Full Event Interpretation. The plots show the best candidate for each event. The external classifiers were trained on a mono-generic Monte Carlo sample and were applied to one million B meson pairs after a correct signal-side reconstruction of $B_{sig} \rightarrow J/\Psi K_S^0$. The output for B^0 (\bar{B}^0) is shown in blue (red). 40

List of Tables

| | |
|---|----|
| 2.1. Comparison of machine parameters between KEKB and SuperKEKB. Taken from [9]. | 5 |
| 6.1. Comparison of individual and total effective efficiencies between Belle II and Belle on Monte Carlo data [7]. The Flavor Tagger for Belle II was trained and applied to one million B meson pairs after the signal-side reconstruction of $B_{sig} \rightarrow J/\Psi K_S^0$. The results are averaged over 10 independent datasets. | 36 |
| 6.2. Results for individual and total effective efficiencies for the Flavor Tagging with included categories of the Full Event Interpretation. The Flavor Tagger was trained and applied to one million B meson pairs after the signal-side reconstruction of $B_{sig} \rightarrow J/\Psi K_S^0$. The results are averaged over 10 independent datasets. | 38 |
| A.1. List of track level variables for direct and secondary electron candidates. | 44 |
| A.2. List of track level variables for direct and secondary muon candidates. | 45 |
| A.3. List of track level variables for kaon candidates. | 46 |
| A.4. List of track level variables for slow and high momentum pion candidates. | 47 |
| A.5. List of track level variables for lambda candidates. | 48 |
| A.6. List of event level variables. | 48 |
| A.7. List of event level variables integrated with the Full Event Interpretation. | 49 |

Danksagung

Zunächst möchte ich Prof. Dr. Thomas Kuhr für die Übernahme des Referates und die vielen hilfreichen Diskussionen danken.

Darüber hinaus danke ich Prof. Dr. Michael Feindt für die Übernahme des Korreferats und die Möglichkeit am Institut für Experimentelle Kernphysik meine Masterarbeit schreiben zu dürfen.

Mein besonderer Dank geht an Dr. Pablo Goldenzweig für die hervorragende Betreuung während der gesamten Arbeit.

Zudem möchte ich mich für die angenehme Atmosphäre bei allen Mitgliedern der B-Gruppen bedanken. Insbesondere möchte ich Thomas Keck hervorheben, der mir stets mit Rat zur Seite stand und die Arbeit korrekturgelesen hat. Des Weiteren danke ich Markus Prim für das Korrekturlesen.

Danke auch an Daniel Kühn für seine fachfremden Hinweise.

Zum Schluss möchte ich meiner Freundin Ines danken, die mich stets während meines Studiums unterstützt hat.

Erklärung

Ich versichere, dass ich diese Arbeit selbstständig verfasst habe und keine anderen als die angegebenen Quellen und Hilfsmittel benutzt habe, die wörtlich oder inhaltlich übernommenen Stellen als solche kenntlich gemacht und die Satzung des KIT zur Sicherung guter wissenschaftlicher Praxis in der gültigen Fassung vom 17.05.2010 beachtet habe.

Karlsruhe, den 29.04.2015, _____
Moritz Gelb

